Valorizing Coffee Waste into N,P,O Heteroatom-Doped Carbons for Metal-Free Electrocatalysis

Journal:	*Chemistry of Materials*
Manuscript ID	cm-2025-02518m.R2
Manuscript Type:	Article
Date Submitted by the Author:	n/a
Complete List of Authors:	Lanero, Francesco; University of Padova Department Industrial Engineering di Giulian, Alissa; University of Padova Department Industrial Engineering Scettri, Anna; University of Padova Department Industrial Engineering Magnano, Elena; Istituto Officina dei Materiali Consiglio Nazionale delle Ricerche, IOM Píš, Igor; Istituto Officina dei Materiali Consiglio Nazionale delle Ricerche Napal Azcona, Ilargi; Istituto Officina dei Materiali Consiglio Nazionale delle Ricerche, Casella, Girolamo; Universita degli Studi di Palermo, Dipartimento di Scienze della Terra e del Mare Carlotto, Silvia; Università degli Studi di Padova, Department of Chemical Sciences Moretti, Elisa; Università Ca' Foscari Dipartimento di Scienze Molecolari e Nanosistemi, Department of Molecular Sciences and Nanosystems Carturan, Sara; University of Padua Department of Physics and Astronomy Alam, Parvez; Roma Tre University Department of Sciences Benedetto, Antonio; Roma Tre University Department of Sciences; University College Dublin, School of Physiscs Zorzi, Federico; Centro di Analisi e Servizi per la Certificazione (CEASC), University of Padua Famengo, Alessia; CNR, Institute of Condensed Matter Chemistry and Technologies for Energy (ICMATE) Ta, Xuan Minh Chau; The University of Sydney Faculty of Engineering, Faculty of Engineering Tran, Thi; The University of Sydney Faculty of Engineering, Faculty of Engineering Tricoli, Antonio; The University of Sydney, School of Biomedical Engineering Sgarbossa, Paolo; Universita degli Studi di Padova, Deaprtment of Chemical Process Engineering Bertani, Roberta; Università degli Studi di Padova Dipartimento di Ingegneria Industriale, Dipartimento di Processi Chimici dell'Ingegneria, Università di Padova Nappini, Silvia; Istituto Officina dei Materiali Consiglio Nazionale delle Ricerche, IOM

Valorizing Coffee Waste into N,P,O Heteroatom-Doped Carbons for Metal-Free Electrocatalysis

Francesco Lanero [a], Alissa di Giulian [a], Anna Scettri [a], Elena Magnano [b], Igor Píš [b#], Ilargi N. Azcona [b,c], Girolamo Casella [d], Silvia Carlotto [e,f,g], Elisa Moretti [h], Sara Maria Carturan [i,l], Parvez Alam [m], Antonio Benedetto [m,n,o], Federico Zorzi [p], Alessia Famengo [f], Xuan M. C. Ta [q], Thi T. K. Tran [q], Antonio Tricoli [q], Paolo Sgarbossa [a,g], Roberta Bertani [a,f,g], and Silvia Nappini [b*]*

[a] Department of Industrial Engineering, UNIPD, Padova, 35131, Italy

[b] CNR - Istituto Officina dei Materiali (IOM), Trieste, 34149, Italy

[c] Physics Department, UNITS, Trieste, 34127, Italy

[d] Department of Earth and Marine Sciences, UNIPA, Palermo, 90123, Italy

[e] Department of Chemical Sciences, UNIPD, Padova, 35131, Italy

[f] CNR - Institute of Condensed Matter Chemistry and Technologies for Energy (ICMATE), Padova, 35127, Italy

[g] CIRCC - Interuniversity Consortium Chemical Reactivity and Catalysis, Padova Research Unit, Bari, 70126, Italy

[h] Department of Molecular Sciences and Nanosystems, Ca' Foscari University of Venice, Mestre, Venice, 30172, Italy

[i] Department of Physics and Astronomy, UNIPD, Padova, 35131, Italy

[l] INFN National Laboratories, Legnaro, 35020, Italy

[m] Department of Science, University of Roma Tre, Rome, 00146, Italy

[n] School of Physics, University College Dublin, Dublin D04 N2E5, Ireland

[o] Conway Institute of Biomolecular and Biomedical Research, University College Dublin, Dublin D04 N2E5, Ireland

[p] CEASC (Centro di Analisi e Servizi per la Certificazione), University of Padova, 35121 Padova, Italy

[q] Nanotechnology Research Laboratory, Faculty of Engineering, University of Sydney, NSW 2006, Australia

* Email: nappini@iom.cnr.it

* Email: roberta.bertani@unipd.it

Abstract

Spent coffee grounds were valorized as a renewable feedstock to prepare N, P, and O co-doped activated carbons via pyrolysis, targeting the development of metal-free electrocatalysts for the oxygen reduction reaction (ORR). Hexachlorocyclotriphosphazene (HCCP) was used as a doping agent, and the influence of different porosity activators such as NH_4HCO_3, KOH, and oxalic acid, was studied. This work employs NH_4HCO_3 as a benign, metal-free activator and secondary nitrogen source, compared against conventional porosity agents. Among the mild activators, NH_4HCO_3 simultaneously provided nitrogen and released NH_3 and CO_2, while oxalic acid generated a clean CO_2 stream, both contributing to mesoporous structure formation. XPS confirmed the successful incorporation of N and P into the carbon matrix, with a high fraction of graphitic nitrogen enhancing conductivity and catalytic activity. Raman spectroscopy, TEM, and XRD analyses revealed predominantly sp^2-hybridized, turbostratic carbon, with higher structural order at 900 ˚C compared to 700 ˚C. The combined effect of pyrolysis temperature, HCCP, and

NH_4HCO_3 produced mesoporous, nitrogen-rich graphitic carbon structures with promising ORR performance, demonstrating a green strategy that maximizes atom economy, minimizes energy input and waste, and transforms low-value biomass into high-performance metal-free electrocatalysts.

Introduction

Heteroatom doped biomass-derived activated carbons represent quite intriguing materials, due to the wide variety of tunable properties induced in the graphitic skeleton by the introduction of nitrogen, phosphorus, sulfur, oxygen, or boron. These heteroatoms interact with the carbonaceous structure either altering the charge distribution or the morphology[1], making these materials suitable for specific applications, encompassing environmental remediation with enhanced absorption capacities for pollutants[2–5] and gases[6], energy storage with improved performance in supercapacitors[7–15] and batteries[16–21], as well as catalysis[22–27], including oxygen reduction reactions (ORR) in fuel cells and oxidation reactions[28–32]. Nitrogen (N)-doping has been extensively investigated due to its ease of incorporation into the carbonaceous lattice, having N and carbon (C) similar atomic radii (0.65 Å and 0.70 Å, respectively). Furthermore, higher electronegativity of N (3.04) with respect to C (2.55) results in the formation of basic sites, which can affect the activity in catalytic processes such as hydrogenations and increase the absorption of acidic gases, i.e., CO_2 [33–35]. Phosphorus (P)-doping, due to its larger atomic radius (0.98 Å), compared to carbon, and its lower electronegativity (2.19), induces extensive defects formation, providing the formation of acidic sites together with a higher electron-donating ability than N. This results in a more metal-

like electronic structure within the carbonaceous framework, thereby improving the electrochemical properties[36–43]. Oxygen (O)-doping converts the hydrophobic nature of carbonaceous materials into hydrophilic, thus increasing both the wettability of carbon electrodes in aqueous electrolyte solutions and the physisorption-based hydrogen storage capacity[44–47]. Sulfur atom is an electron-rich element with a lone pair of electrons, thus improving the surface properties of carbon materials. S-doping in the carbon framework has been reported to induce a remarkable increase in electrode polarization, leading to higher charge transfer kinetics and higher specific capacitance[9,48–51]. Boron has been investigated in carbon materials to enhance their oxidation stability and electrochemical behavior. B-doping has been reported to modify the electrochemical capacitance and the electronic structure of the materials and increase the number of hole-type charge carriers, enhancing their conductivity[52–57]. Co-doping generally exhibits a synergistic effect on the chemical, electrical, and morphological properties of carbon materials, enabling a fine tuning of the properties and leading to the formation of high spin and charge densities within the carbon network. It has been reported that N-P co-doping induces local curvature in the planar graphitic sheets, thus affecting the electrochemical and mechanical properties of sp^2 layered carbon. Increasing the local reactivity with the formation of highly localized states, which is attractive for electrochemical redox reactions, improves surface wettability and enhances electronic conductivity and specific capacitance[58]. Additionally, the presence of P-dopant can create a protective layer on the carbon surface, suppressing the formation of unstable oxygen-containing surface groups[59]. Furthermore, N-O co-doping can create a larger polarized surface with increased wettability, facilitating fast electrolyte ion migration rates and improving

electrochemical properties for carbon-based supercapacitors[47,60,61]. Appropriate N-O and N-P co-doping have also been reported to generate suitable pore distribution, leading to improved electrochemical, absorption, and catalytic performance in oxygen reduction or oxygen evolution reactions[1].

Heteroatom doping for carbonaceous materials can be achieved through two approaches, *post-treatment* or *in situ* doping. Post treatment doping usually requires a pre-carbonization of the biomass in the presence of porosity activator (i.e. KOH, K_2CO_3, NaOH), followed by treatment with the doping agents such as phosphoric acid, phytic acid, melamine, urea, thiourea, boric acid, etc.[62]. On the contrary, *in situ* doping involves the direct carbonization of the biomasses, which inherently contains different amounts of heteroatoms depending on their origin, in the presence of the doping agent[9]. The selection of the doping element and method is guided by the intended application and desired properties of the activated carbon, aiming to tailor the electronic structure, physical, chemical and morphological properties[63].

Recently, to achieve NP co-doping, phosphazenes (compounds based on the -P=N skeleton) have been investigated for *in situ* processes due to their unique advantage of enabling macromolecular substitution synthesis. This approach allows a wide variety of organic side groups to be linked to the inorganic skeleton, broadening their potential applications[64,65]. Different strategies have been followed:

i. Suitable functionalization of poly-dichloro-phosphazene to achieve crosslinked phosphazene materials bearing holes as a template for carbons with controlled morphology and composition[66–71];

ii. Carbonization of preformed cyclomatrix polyphosphazenes to achieve hollow carbon nanospheres to apply in pollutant removal[3,72,73], CO_2 capture[74], high-performance supercapacitor application[75,76], metal- or precious metal-free electrochemical catalysts in ORR[77,78]. In all cases, the materials are characterized by hierarchical porosity, good wettability and presence of heteroatoms to improve dipolar interactions with ions on the electrode surface;

iii. Preparation of heteroatom-doped core/shell carbonaceous materials with designed homogeneous metal-nanoparticles distribution for high-performance energy storage systems in electrochemical power devices[79]; for the efficient oxygen evolution reaction[80–82], lithium-ion batteries[20] and as electrochemical sensors[83].

To the best of our knowledge, in most cases, the only carbon source has been represented by the organic moieties attached to the P atoms of phosphazenes. Only a few reports describe the carbonization of phosphazenes in the presence of additional carbon sources[29,84].

Herein, we report the synthesis of a series of N, P, O co-doped carbonaceous materials derived from hexachlorocyclotriphosphazene (HCCP) in the presence of spent coffee grounds as carbon source[85], employing either a one-step (*in situ*) or two-step (*post-treatment*) strategy. The influence of different porosity activators, including KOH, oxalic acid, and NH_4HCO_3, on the chemical composition, morphology, and electrocatalytic properties of the resulting carbons was systematically investigated. Finally, the oxygen reduction reaction (ORR) activity of the co-doped activated carbons was evaluated, revealing their excellent potential as metal-free electrocatalysts for environmental energy conversion applications.

Experimental Section

Reagents and Raw Materials

Waste coffee grounds were collected from Dersut Caffè S.p.A. (SCG). They are a mixture of Robusta and Arabica qualities that appear as dark brown flakes with a spongy texture (**Figure S1**). The grounds were dried at 110 ˚C for 24 h and stored under vacuum to prevent mold formation. A preliminary elemental analysis by EDS (average of five samples) gave the following compositions by weight: C 59.6 %, N 2.5 %, O 37.2 %, and K 0.7 % w/w, similar to the SCG compositions previously reported[85]. Before use, the SCG powder was ground in a Retsch mixer mill for 3 min. Potassium hydroxide (KOH), oxalic acid $(COOH)_2$ and ammonium hydrogen carbonate, NH_4HCO_3, were purchased from Merck and used as received. Hexachlorocyclotriphosphazene ($N_3P_3Cl_6$, HCCP) was obtained from Merck and purified by sublimation.

Preparation of the Activated Carbon

Blends of spent coffee ground, HCCP (as a doping agent), and activating agent (AA) were pyrolyzed in a covered Al_2O_3 crucible under inert atmosphere (N_2 flow rate 5 lt/min) from room temperature to 700 ˚C or 900 ˚C at a heating rate of 10 ˚C/min for 2h in a muffle furnace. Three porosity activating agents were used: KOH, oxalic acid, and NH_4HCO_3. For KOH, the preparation was carried out in two separate steps: first, a pyrolysis of SCG alone or mixed with HCCP at a 1:1 ratio (w/w), followed by a second pyrolysis step of the dried mixture with KOH added at 1:1 w/w ratio (dissolved in water). For oxalic acid and ammonium bicarbonate, the pyrolytic processes were carried out in a single step. The SCG alone or the SCG/HCCP (1:1 w/w) mixture was treated

with the activating agent either by direct mixing in a mortar or by impregnation with aqueous solutions, followed by pyrolysis of the resulting material. After cooling, the pyrolyzed samples were washed with deionized water and, if necessary, treated with a solution of 0.1 M HCl until neutral pH was reached. The activated carbons (ACs) were then collected and stored in airtight bottles for further analysis. The sample labels, experimental conditions, and compositions are listed in **Table 1**.

Table 1. Sample designations, activating agents (AA), pyrolysis temperatures (T), and yields for activated carbons prepared from SCG and SCG/HCCP mixtures.

Sample	Components	AA	T (°C)	Yield[a]	Sample	Components	AA	T (°C)	Yield[a]
1A	SCG alone	-	700	25	**2A**	SCG/HCCP	-	700	30
1B	SCG alone	-	900	18	**2B**	SCG/HCCP	-	900	20
1C	SCG alone	KOH	700	18	**2C**	SCG/HCCP	KOH	700	28
1D	SCG alone	KOH	900	15	**2D**	SCG/HCCP	KOH	900	25
1E	SCG alone	Oxalic acid	700	23	**2E**	SCG/HCCP	Oxalic acid	700	25
1F	SCG alone	Oxalic acid	900	20	**2F**	SCG/HCCP	Oxalic acid	900	20
1G	SCG alone	NH_4HCO_3	700	20	**2G**	SCG/HCCP	NH_4HCO_3	700	24
1H	SCG alone	NH_4HCO_3	900	18	**2H**	SCG/HCCP	NH_4HCO_3	900	20

[a] Pyrolysis experiments were repeated at least three times to evaluate reproducibility, with similar yields obtained in each case.

Textural and Chemical Characterization

The morphology of the samples was examined by Environmental Scanning Electron Microscopy (ESEM, Quanta 200 FEI) (**Figure S1**). Semi-quantitative elemental analysis was performed using the integrated energy-dispersive X-ray spectroscopy (EDS) system. The chemical composition of

the samples derived from EDS is summarized in **Table S1**. The microstructure of the samples was characterized by transmission electron microscopy (TEM) and high-angle annular dark-field scanning transmission electron microscopy (HAADF-STEM) using a JEOL F200 TEM operated at 200 kV. Elemental analysis and mapping were performed using a JEOL 100 mm^2 silicon drift energy dispersive X-ray spectrometer (EDS). Samples were prepared using lacey carbon grids with a 400-mesh size.

X-ray photoelectron spectroscopy (XPS) was carried out at the BACH beamline of CNR at the synchrotron radiation facility Elettra (Trieste, Italy). The beamline is equipped with a hemispherical electron analyzer (Scienta R3000) positioned at an angle of 60° relative to the X-ray incidence direction. Binding energies (BE) were referenced against the Au $4f_{7/2}$ (84.0 eV) signal from polycrystalline Au foil in electrical contact with the samples. The X-rays were linearly polarized with the polarization vector parallel to the scattering plane. Photoemission spectra were collected using a photon energy of 730 eV and a total instrumental resolution of 0.2 eV. The C 1s, O 1s and N 1s spectra were fitted with Voigt functions, while the P 2p spectra were fitted with Voigt doublets. The P $2p_{3/2}$ – P $2p_{1/2}$ spin-orbit splitting and intensity ratio were fixed at 0.88 (eV) and 2:1, respectively. A Shirley-type background was applied where appropriate; otherwise, a linear background was subtracted. Atomic concentrations were determined from the integrated peak intensities corrected for the incident X-ray flux and relative sensitivity factors (**Table S2**).

Fourier Transform Infrared spectroscopy (FTIR) spectra of the carbon powders were obtained on a Perkin Elmer Spectrum 100 instrument in ATR mode. For each sample 32 scans were recorded in the range 4000-400 cm^{-1} in the transmittance mode with a resolution of 4 cm^{-1}.

Raman spectra were recorded using a continuous wave linearly polarized instrument (model DRX, Thermo Scientific with an excitation laser having 514.5 nm wavelength, 2.41 eV, 16 mW power). The laser beam was focused by a 100× objective lens, resulting in a spot of about 1 μm in diameter (**Tables S4a–c**).

1D-$^{13}C\{^{1}H\}$ and 1D-$^{31}P\{^{1}H\}$ MAS-NMR experiments were acquired on a Bruker Avance III spectrometer at a magnetic field strength of 7.0 T using a standard-bore probe at 23˚C. The ^{1}H, ^{13}C and ^{31}P Larmor frequencies were 300 MHz, 75.6 MHz and 121.5 MHz, respectively. The samples were placed into a 4.0 mm ZrO_2 rotor equipped with Kel-F cap and diluted with metakaolinite to properly tune the probe and spun at a magic-angle spinning frequency of 10 kHz for 1D-$^{13}C\{^{1}H\}$ and at 6kHz for 1D-$^{31}P\{^{1}H\}$. The ^{13}C signals were enhanced by cross-polarization CP-MAS with 2 ms of contact time and 2.4 μs of ^{1}H 90˚ pulse, with SPINAL-64 proton decoupling. A two-second recycling delay between transients was set for 20000 transients.

^{31}P signals were enhanced by cross-polarization CP-MAS with 5 ms of contact time and 3.4 μs of ^{1}H 90˚ pulse with SPINAL-64 proton decoupling, a 2 s recycle delay between transients was set for a number of 20000 transients. 31P SPE MAS NMR (single pulse) with 1H decoupling was also acquired with a 5 s recycle delay and 3000 transients. ^{13}C spectra were referenced to Adamantane at 38.48 ppm with respect to TMS and ^{31}P to ammonium dihydrogen phosphate at 0 ppm. NMR data analysis, deconvolution, and fitting were carried out using Bruker TopSpin and DMfit vs64.

Thermogravimetric analysis (TGA) of the samples were realized with SDT Q600 TA instrument under air, from 30 ˚C to 1000 ˚C at a heating rate of 10 ˚C/min or with a Netzsch STA 449 F1 Jupiter Thermal Analyzer in Al_2O_3 crucibles, heating from 25 ˚C to 1000 ˚C at 10˚C/min under N_2

atmosphere (100 ml/min). Data has been processed via Netzsch Proteus Thermal Analysis software (**Table S6**).

The textural properties of the samples were studied by N_2 adsorption at 77 K with a static volumetric instrument (ASAP2020, Micromeritics) over a relative pressure range of approximately 10^{-6} to 0.998 (p/p_0). Prior to the analysis, all samples were degassed at 423 K for 18 h under vacuum to completely remove any trace of adsorbed water. MicroActive software available from Micromeritics was used to derive the specific surface area of the samples by the standard Brunauer-Emmett-Teller (BET) method using N_2 adsorption data in the relative pressure range from 0.002 to 0.30, and the pore size distribution (PSD) using the Barrett-Joyner-Halenda (BJH) method applied to the desorption branch of the isotherms. The same software was used to apply the two-dimensional non-local density functional theory specific for heterogeneous surfaces (HS-2D-NLDFT) to evaluate surface area (S_{NLDFT}), PSD extended to the micropore range (width < 2 nm), micropore volume ($V\mu$), and total pore volume. The total pore volume was also estimated from the amount of N_2 adsorbed at a relative pressure of about 0.98. Textural parameters are summarized in **Table S7**.

The proximate analysis has been carried out according to ASTM D 5142 – 04. For moisture analysis, 500 ± 1mg of the samples were dried at 105 ± 2˚C in air to obtain constant mass. For determination of ash content, 500 ± 1mg of the samples were heated in a muffle furnace at 500˚C for 1h and at 750˚C for 2h. To estimate volatile content, 500 ± 1mg of the samples were heated at a heating rate of 50˚C/min to 900 ± 20˚C for 7 min. The fixed carbon was calculated by means of

the relationship FC = 100% - (V + A + M) where FC, V, A, and M are the contents (wt.%) of fixed carbon, volatile, ash, and moisture, respectively. The results are reported in **Table S8**.

X-ray diffraction (XRD) spectra have been recorded to characterize the samples using a PANalytical X'Pert Pro diffractometer equipped with a Co X-ray tube and a real-time multiple strip (RTMS) detector (X'Celerator). The results are summarized in **Table S9**.

Electrochemical Characterization

The electrochemical performance of the synthesized catalysts was evaluated using a standard three-electrode electrochemical setup (**Figure S9**). A mini hydrogen reference electrode (Mini Hydroflex, ET096, EdaQ) was used as a reference electrode, and a 1 mm diameter platinum wire served as counter electrode. The working electrode was a glassy carbon substrate (PalmSens), onto which the catalyst was deposited by drop-casting. The catalyst ink was prepared by dispersing 5 mg of the synthesized catalyst powder in 1 mL of a mixed solvent containing 50 µL of 5 wt% Nafion™ solution (Sigma Aldrich) and 950 µL of Milli-Q water. The mixture was sonicated to ensure a homogeneous suspension. A total of 120 µL of the ink (60 µL on each side) was drop-cast onto the glassy carbon electrode and subsequently dried at approximately 100 ˚C. This resulted in a catalyst loading of 0.6 mg cm^{-2} for all samples. Cyclic voltammetry (CV) measurements were performed in 0.1 M KOH aqueous solution. For ORR studies, the electrolyte was initially saturated with O_2 to evaluate catalytic activity, followed by N_2 purging to record baseline measurements. All the CV measurements were carried out under continuous gas flow

using a PalmSens4 potentiostat, operating over a potential range of −5 V to +5 V and a current range of 100 pA to 10 mA, providing high resolution and low-noise performance.

Results and Discussion

Preparation and Chemical Characterization

As reported in **Table 1**, a series of N, P, and O doped activated carbons have been prepared from SCG through pyrolytic processes carried out at different temperatures in the presence of HCCP as N and P source. In order to investigate the development of porosity and its relationship with doping efficiency, a series of different activating agents were introduced using two procedures: (i) dry mixing in a mortar and (ii) impregnation with aqueous solutions of the activators. Among the activating agents, NH_4HCO_3 was employed either as additional N source or as gaseous NH_3 and CO_2 source without leaving metal residues in the final product. Oxalic acid was used as a clean source of CO_2. The results have been compared with those achieved with KOH, widely used as an activating agent in the pyrolytic processes carried out either on SCG alone or SCG/HCCP mixtures. The activated carbon obtained from the pyrolysis of the SCG/HCCP mixture under the experimental conditions used in this study has, to the best of our knowledge, not been previously investigated.

A reasonable HCCP decomposition pathway explaining N and P incorporation during pyrolysis is discussed in the Supporting Information, supported by the identification of intermediate species through positive-ion mass spectra of both bare HCCP (**Figure S10**) and HCCP mixed with SCG (**Figure S11**) at 600 ˚C under N_2 atmosphere.

The effect of pyrolysis was clearly evident: increasing the temperature from 700˚C to 900˚C the yields were slightly reduced (**Table 1**), while the carbon content increased with the temperature (**Table S1**). As reported in **Figure S2**, the elemental composition of the resulting materials, expressed as % w/w P/C and N/C ratios, was influenced by both the pyrolysis temperature and the activating agent. In particular, in the absence of any AA, the increase of the temperature showed a significant decrease in N content, as also observed in the presence of KOH[59] and oxalic acid. In contrast, the pyrolytic processes carried out in the presence of NH_4HCO_3 resulted in a significant increase in the N content, as expected. The P content, on the other hand, appeared to be less influenced by the experimental conditions and generally increased in the ACs at 900 ˚C. The samples prepared from SCG/HCCP mixtures showed an increase of both N and P content at both pyrolysis temperatures, especially in the case of NH_4HCO_3 used as AA at 700 ˚C. However, it should be noted that during the pyrolysis NH_4Cl was formed (collected and identified through FTIR by comparison with a reference sample), thus reducing the total N amount in the final activated carbons, giving in general an increase in P content higher than N.

It is worth noting that the two preparation procedures, dry mixing and impregnation, did not reveal significant differences in the final composition of the samples. On the contrary, the morphology appeared significantly different, resulting in a more corrugated texture in the latter case (**Figure S1**). Another relevant observation concerned the discrepancy between the EDS results and XPS analytical data, the latter indicating a lower N content and, in most cases, a higher P amount (**Figure S2**). These differences are due to the different probing depth of the two methods (1–3 μm in EDS vs 5 nm in synchrotron-based XPS)[61,86]. A deeper penetration in EDS analysis

results in a higher average concentration of N and a lower P content, suggesting that phosphorus is predominantly present on the external surface of the biochar, while nitrogen in the internal part, as shown in **Figure 1**. The observation was in agreement with the deconvolution of the N 1s spectra (**Figure 2** and **Table S3b**) where four peaks at 398.3 ± 0.1, 399.6 ± 0.2, 400.7 ± 0.2 and 402.3 ± 0.3 eV, ascribed to pyridinic N (bound to two C atoms), pyrrolic N (bound to two C atoms and one H atom), graphitic N (bound to three C atoms) and oxidized N, respectively, have been distinguished, being the graphitic one the most abundant (in most cases 38% or more). Notably, the high content of graphitic N is typically associated with enhanced electrical conductivity of the carbon, resulting from N-doping within the sp^2-carbon framework, which is beneficial for electrocatalytic applications, while the pyridinic and pyrrolic moieties have been reported to favor the pseudocapacitance of the electrode materials[67,86,87]. P 2p XPS spectra (**Table S3c**) revealed the presence of P-O species with different degrees of reduction. The spectra were resolved into three main components. The P 2p component with P $2p_{3/2}$ at 134.7 ± 0.2 eV could be attributed to O-P(=O)$(OH)_2$; the middle component (P $2p_{3/2}$ at 133.5 ± 0.3 eV) to overlapping signals from C-P(=O)$(OH)_2$ and C_2-P(=O)OH functional groups; and the low BE component (P $2p_{3/2}$ at 132.1 ± 0.3 eV) to C_3-P=O[88,89]. The extra peak at BE >136 eV exhibited pronounced charging upon X-ray irradiation, indicating the presence of non-conducting native phosphorus oxides and suboxides segregated on the surface of the AC. Since these oxides are not an integral part of the AC, they were excluded from the compositional analysis of the AC. We could not exclude the presence of P-N or P=N moieties, as their P 2p spectra overlap with those of P-O groups. However, based on

the observed P/N and P/O intensity ratios and their variations between the samples, it can be concluded that the P-O groups were the dominant species.

It has also been observed that an increase in oxygen content is associated with slight incorporation of oxygenated species, such as carbonyl, phenolic, carboxylic,[90] and P-O bonds[91], into the carbon structure (**Figure 1**), although, due to the high surface sensitivity of XPS, a considerable part of the detected oxygen signal may originate from species formed on the AC surface after air exposure.

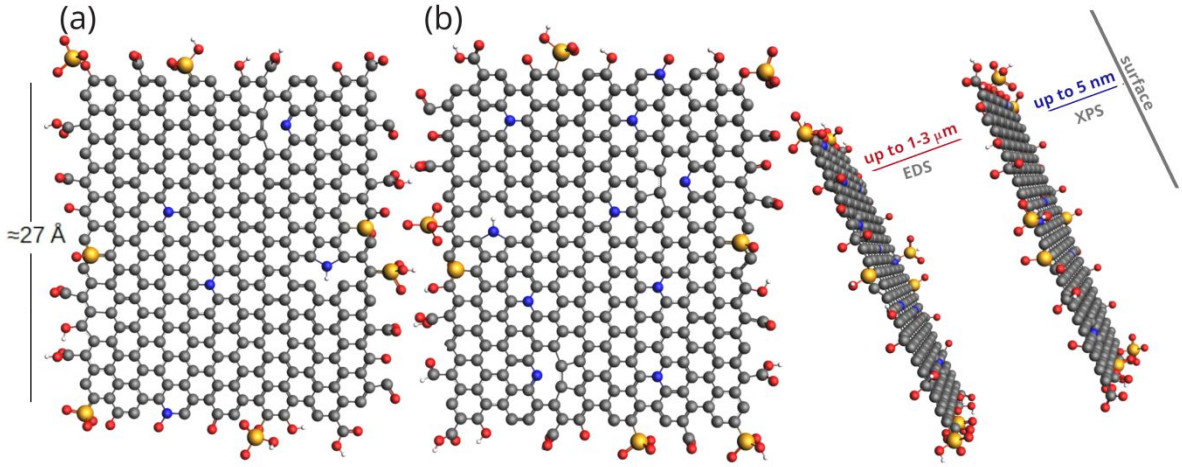

Figure 1. Schematic model of the activated carbon surface (a) and near-surface heteroatom doping (b), estimated from XPS and EDS data of sample **2H**. The illustration on the right indicates the approximate detection depths of each technique. Atom colors: grey = carbon, red = oxygen, blue = nitrogen, yellow = phosphorus.

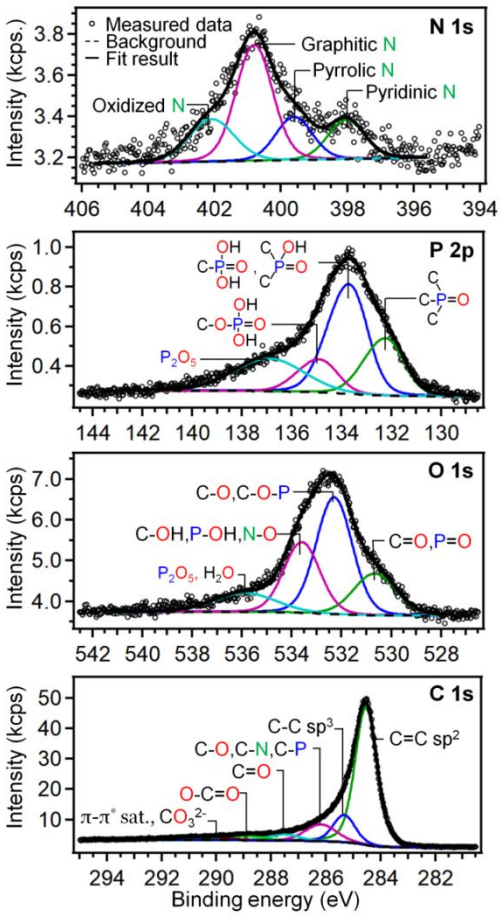

Figure 2. XPS spectra of the N 1s, P 2p, O 1s, and C 1s regions for activated carbons (sample **2H**, SCG/ HCCP, NH_4HCO_3, 900 ˚C) and corresponding deconvolution fits.

The ATR-FTIR spectra of the samples were also recorded; however, due to the extremely low intensity of the signals, the results are not shown. Nonetheless, features attributable to C=O stretching, C=C vibrations of aromatic rings, and out-of-plane C–H bending typical of aromatic structures were observed. In samples with higher phosphorus content, additional bands corresponding to P–O moieties of phosphates and P–O–C bonds of acidic phosphate esters were detected[92], whereas the characteristic signals of the HCCP ring were absent.

A more detailed and reliable analysis was achieved using Raman spectroscopy. Raman spectra of the carbonaceous materials were collected with an excitation wavelength of 514 nm, which has strong selectivity towards the π states of sp^2-hybridized carbon species. The spectra exhibited two characteristic bands at approximately 1350 and 1590 cm^{-1}, corresponding to the D and G bands, respectively. The D band is associated with the vibrational mode of microcrystalline graphite, which becomes Raman-active only in the presence of structural defects in graphene planes, while the G band is linked to defects in stacked graphene sheets[67,68,70–72,74,78–80,83].

The spectra in the range of 1000-1600 cm^{-1} (**Figure 3**, **Table S4b**) were deconvoluted into four contributions (D1, D3, D4, and G1, centered at ~1350, ~1540, ~1300, and ~1590 cm^{-1}, respectively), providing information on the degree of structural order in the carbon samples. In the literature[93], the parameters R1 = A_{D1}/A_{G1} and R2 = $A_{D1}/(A_{G1}+A_{D1}+A_{D2})$ have been proposed as reliable indicators of the structural order of carbonaceous materials. These parameters are considered more accurate and less variable than the commonly used A_D/A_G parameter derived from simplified two-component deconvolution (**Table S4a**)[93–96].

It is noteworthy that the D2 band, typically observed in the range 1580-1620 $cm^{-1}$and associated with disordered graphitic structures, was not present in the Raman spectra of the studied samples. The D4 absorption band, attributed to amorphous sp^3-hybridized carbon, was shifted to below 1300 cm^{-1} only in samples prepared at 700 °C[91]. An intense peak at ~1350 cm^{-1}(D1) related to a high density of phonon states near the Brillouin zone corner of the disordered graphite lattice (A_{1g}) was also observed, along with the D3 band related to amorphous carbon. The G1 band, related to the E_{2g} vibrational mode of the graphitic structure, was observed at ~1595 cm^{-1}.

The calculated R2 values for most samples exceeded 0.5, indicating a high defect density. However, the samples prepared at 900˚C showed lower R2 values respect to those prepared at 700˚C. The D3 and D4 bands, related to amorphous carbon, adsorbed molecules, functional groups, and disordered graphite lattice, showed reduced intensity at higher pyrolysis temperatures. Accordingly, the A_{D4}/A_{G1} and A_{D3}/A_{G1} ratios decreased in samples prepared at 900˚C compared to those prepared at 700˚C, indicating a lower content of amorphous carbon and functional groups in the ACs obtained at higher temperature[97]. Overall, the samples can be classified as mainly sp^2 amorphous carbons[93,94]. Although the 900 ˚C treatment promoted a slight increase in graphitic order, the materials remained largely disordered, as confirmed by the high values of A_D/A_G[98] consistent with observations typically reported for biomass-derived carbon materials. In **Figure 4** and **Table S5**, the R2 (ranging from 0.44 to 0.74) and R1 (ranging from 0.79 to 5.77) values, together with the sp^3/sp^2 C1s XPS peak intensity ratio, are reported, indicating the development of graphitic crystallites within the turbostratic structure at higher temperatures[99,100]. The presence of defects can facilitate pseudocapacitive charge storage mechanisms, leading to higher initial capacities. However, the amorphous structure and limited graphitic ordering can result in poor stability during cyclic voltammetry and the formation of an unstable solid-electrolyte interface layer[101].

Second-order overtone and combination Raman absorptions in the region 2200–3400 cm^{-1} were also observed (**Figure 3 and Table S4c**). The 2D band, at ~2700 cm^{-1} is the second order of the D band and typically appears for graphite containing carbons. The splitting of the other bands

changed according to the number of graphene layers stacked along the hexagonal axis and represents a useful parameter for studying short and medium range stacking order.

The A_{2D}/A_G ratio can serve as a useful marker for graphene structure identification, with values higher than 1 typically attributed to monolayer graphene. In all investigated samples, however, the A_{2D}/A_G ratio was lower than 1, and particularly low for carbons prepared at 900˚C, indicating the presence of multilayer structures. Additionally, the presence of defects in the AC structures was further confirmed by the presence of a signal at ~2940 cm^{-1} (D+D' band), attributed to the combination of phonons with different momenta, which requires defects for activation[102,103].

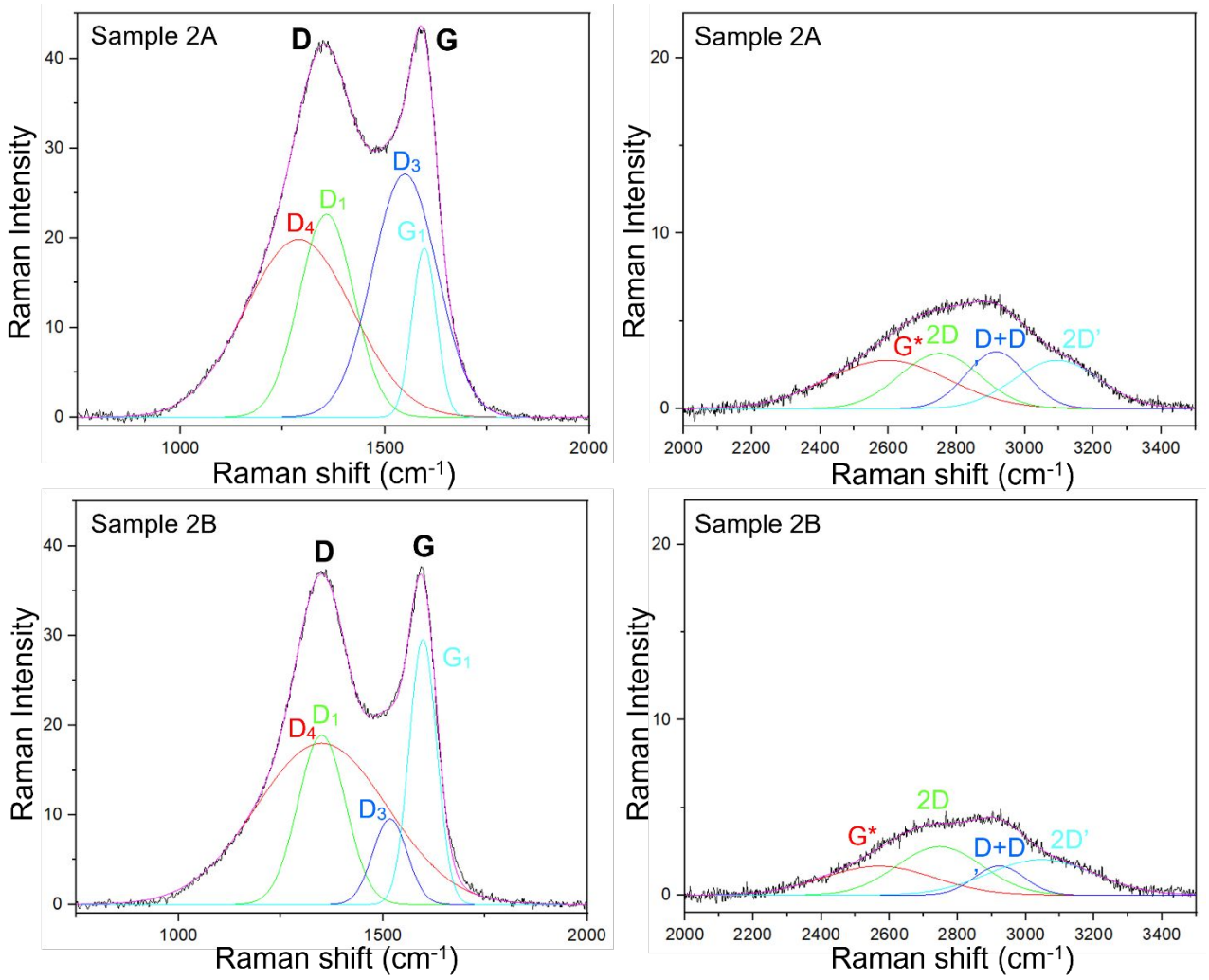

Figure 3. Raman spectra of activated carbons derived from SCG/HCCP prepared at 700 ˚C (sample **2A**) and at 900 ˚C (sample **2B**), shown in the 1000–1750 cm^{-1} and 2200–3400 cm^{-1} regions.

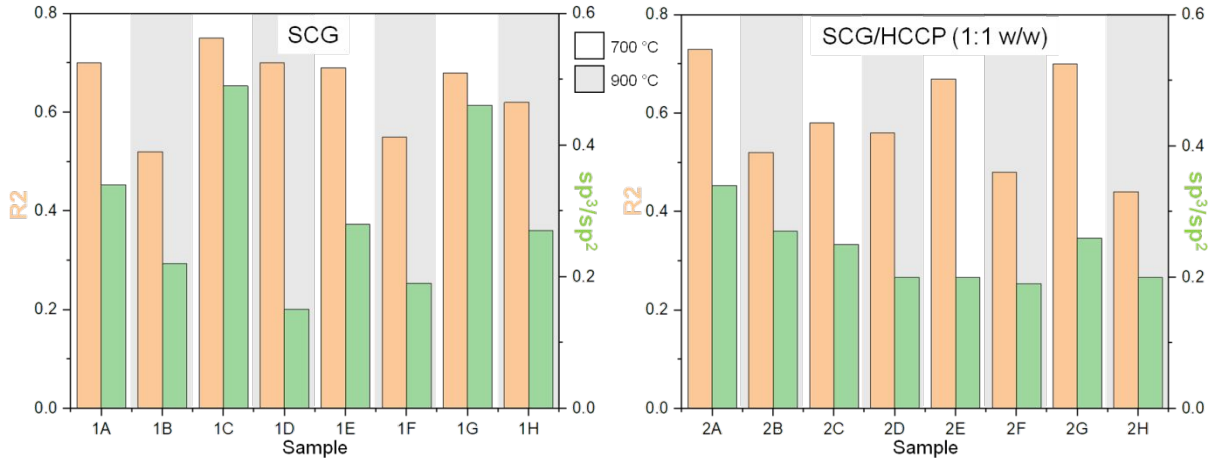

Figure 4. Comparison between the R2 parameter obtained from Raman spectra and the sp^3/sp^2 peak intensity ratio derived from XPS C 1s spectra.

The carbon local structure of samples **2C** and **2H** were investigated by ^{13}C CPMAS NMR (**Figure 5**), to evaluate also the possible presence of surface groups. The lower ^{13}C signal intensity detected for sample **2H** with respect to **2C** in the cross-polarization (CP) spectra (**Figure 5a**) indicated the presence of a lower fraction of ^{13}C nuclei in proximity to protons. Since cross-polarization in NMR relies on the transfer of magnetization from nearby protons (^{1}H) to carbon nuclei (^{13}C), this suggests that sample **2H** contains a smaller proportion of carbon atoms situated in hydrogen-rich environments. Due to the low signal/noise ratio of sample **2H**, the spectral deconvolution was performed only on sample **2C,** using a combination of four main Lorentzian/Gaussian line-shape components (**Figure 5c**, **Table 2**). The main and broad peak at 126 ppm (**Figure 5a**) is characteristic of sp^2-hybridized carbon in condensed aromatic rings[87,89,104], typically attributed to C=C groups in proximity of protonated carbon atoms. The lower intensity resonance at 110 ppm is attributable to protonated aromatic carbons (C_{aro}-H). Two additional broad signals at 141 ppm and 162 ppm are in the chemical shift range of aromatic carbons bonded to nitrogen (C_{aro}-N) and oxygen (C_{aro}-O),

consistent with the presence of phenolic C-OH or lactones and with pyridinic or pyrrolic functionalities[105]. The broad line at 186 ppm originated from C=O resonances of aldehydic, lactone and quinonic moieties. The broadening of the signal could reflect a distribution of sp^2 islands with different sizes. Resonances in the aliphatic region 0-50 ppm were not detected.

^{31}P MAS-NMR spectra for samples **2C** and **2H** (**Figure 5c**) are dominated by a broad signal centered at 0 ppm (**Figure 5b**) arising from the overlapping resonance of several phosphate-like structures (bound to four oxygen atoms) with different degrees of hydration. The peak at 7.0 ppm is due to phosphorus atoms bonded to oxygen atoms in aromatic systems (P-O-Ar). The signal at about 27.6 ppm, not detected for sample **2H**, could be attributed to phosphonate moieties, i.e., compounds with C-P bonding suggesting that phosphorus atoms were directly incorporated in the aromatic rings[106]. The resonance detected at -22.45 ppm for **2C** and the two peaks at 15.5 ppm and 27.1 ppm were tentatively assigned to polyphosphates, usually resonating in the -15 to -30 ppm region[107]. Due to the high chemical shift anisotropy of ^{31}P, several spinning side bands (ssb) of the phosphate signals are present and marked with asterisks.

Table 2. Results of the spectral deconvolution of the ^{13}C CP MAS NMR spectrum of activated carbon sample 2C (SCG/HCCP, KOH, 700 ˚C), using a combination of Lorentzian and Gaussian line-shapes. G/L=1 corresponds to pure Gaussian, and G/L = 0 to pure Lorentzian.

Chemical shift (ppm)	Peak amplitude	Peak width (ppm)	G/L ratio	Peak area (%)
126.03	24.58	18.07	0.5	60.09
162.47	3.72	14.23	0	8.53
186.21	1.07	17.54	0	3.02

141.23	5.86	19.63	0	18.54
109.96	3.45	17.67	0	9.82

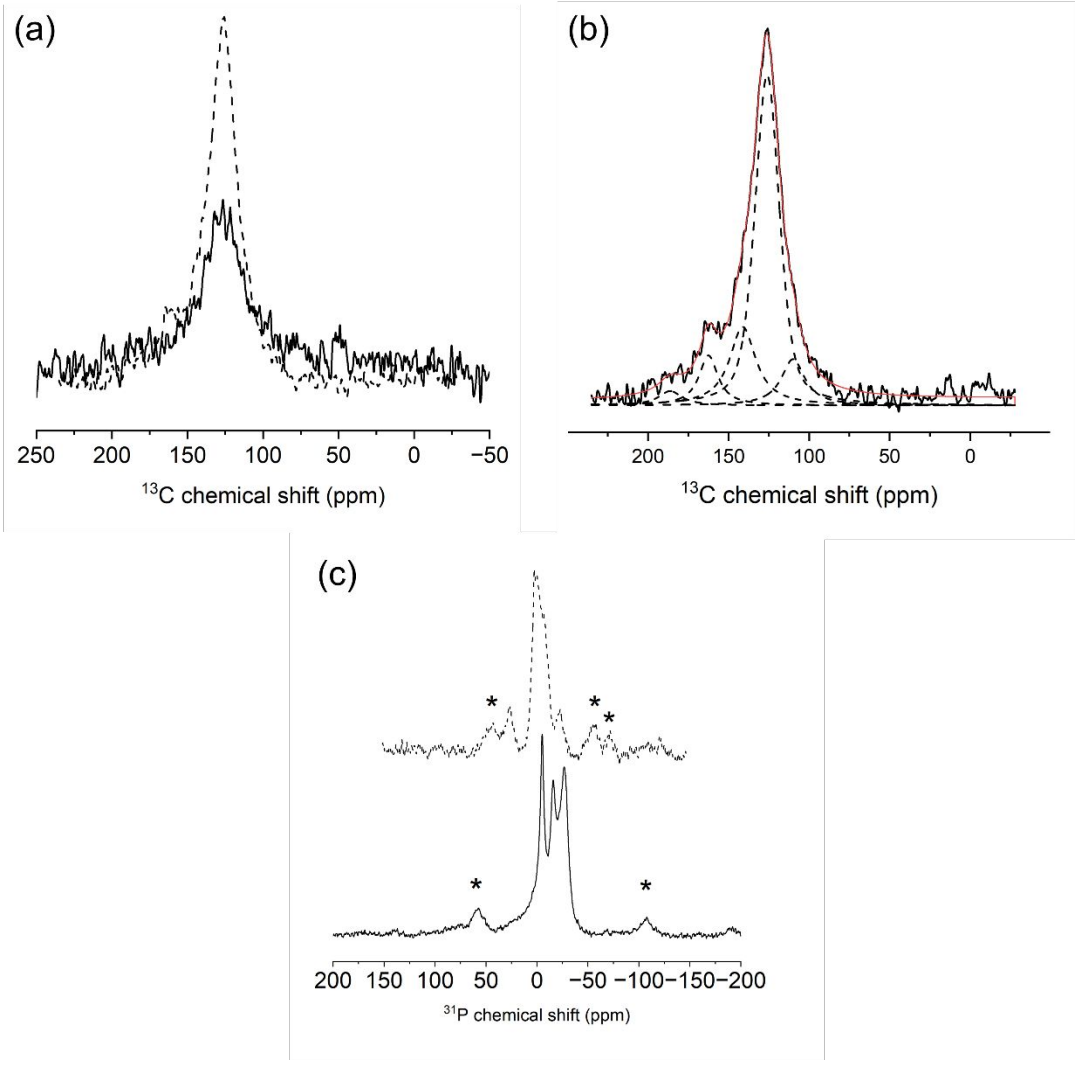

Figure 5. (a) ^{13}C CPMAS NMR of **2C** (dashed) and **2H** (solid). (b) ^{13}C-CPMAS spectrum of **2C** fitted into Gaussian/Lorentzian line-shapes: experimental (black) and model spectrum (red). (c) ^{31}P CPMAS NMR of sample **2C** (dashed) and ^{31}P SPE 2 MAS NMR of **2H** (solid). Due to the higher chemical shift anisotropy of ^{31}P, several spinning side bands (ssb) are present and marked with asterisks (6000 kHz for **2C** and 10000 kHz for **2H**).

The thermal stability has been investigated (**Figure S7** and **Table S6**), by TGA analysis. The TGA curves of all doped carbons showed a similar thermal behavior, characterized by a first weight loss around 100 ˚C due to elimination of moisture and light-weight volatile compounds, such as CO, CO_2 and hydrocarbons formed by degradation of the biomass, potentially catalyzed by the residual metals. This is followed by a minor decrease up to approximately 400 ˚C, and a major degradation step beginning between 400 and 600 ˚C, depending on the specific sample. Up to 550–600 ˚C a limited weight loss (5–10%) was observed. Above this temperature a more pronounced mass loss was detected, due to the decomposition of oxygenated moieties (such as lactones and carbonyls), which release CO_2 and CO above 600 ˚C. The final residue at 800 ˚C ranged from 50 to 75% for all samples, except for the samples activated with KOH, which exhibited lower residue values of 35-40%[2,108].

Physical and Textural Characterization

Inorganic elements such as K, Mg, Ca, and Na, detected in the starting SCG, are known to promote pore formation during pyrolysis, leading to increased surface area and improved adsorption and electrochemical properties. The porosity of the prepared activated carbons was assessed by N_2 adsorption-desorption isotherms (**Figure 6** and **Table S7**). The samples prepared at 700 ˚C exhibited Type I isotherms, characteristic of microporous structures, while those pyrolyzed at 900 ˚C displayed Type IV isotherms with hysteresis, indicative of the development of mesoporosity and hierarchical pore structures[109,110]. This structural evolution, as evident in sample **1H** (**Figure 6**), correlates with high levels of doping and suggests favorable electrochemical performance.

The isotherms of the samples prepared at 700 ˚C showed pronounced N_2 uptake at low relative pressures, indicating a microporous structure (**Figure 6a**). When the pyrolysis temperature was increased to 900 ˚C, the micropores partially transformed into narrow mesopores, likely due to the removal of amorphous carbon. This transformation is suggested by the appearance of hysteresis loops in the isotherms and by pore size distributions obtained using the BJH and HS-2D-NLDFT models (**Figure 6a-b**)[98,101,102,108].

The highest surface areas were achieved when KOH was used as the activating agent. Oxalic acid was also effective, especially in samples **1F** and **2F** at 900 ˚C. This could be due to the reaction of oxalic acid with potassium in the SCG material, forming potassium oxalate. Potassium oxalate has been reported to activate porosity in biomass pyrolysis and is less corrosive than KOH. At high temperatures, potassium oxalate thermally decomposes into K_2CO_3 with CO evolution. Above 700 ˚C, K_2CO_3 decomposes further into K_2O and CO_2, with K_2O being then reduced by carbon to K, exhibiting an activation behavior comparable to KOH[6,111].

Depending on the experimental conditions, NH_4HCO_3 was found to function both as an additional nitrogen source and as a porosity-activating agent, resulting in high surface areas of 1293 m^2/g and 937 m^2/g for samples **1H** and **2H**, respectively, both prepared at 900 ˚C. The high variability and occasionally reduced surface areas observed in the doped carbons are consistent with previous studies and are often attributed to aggregation[75,87,112–115].

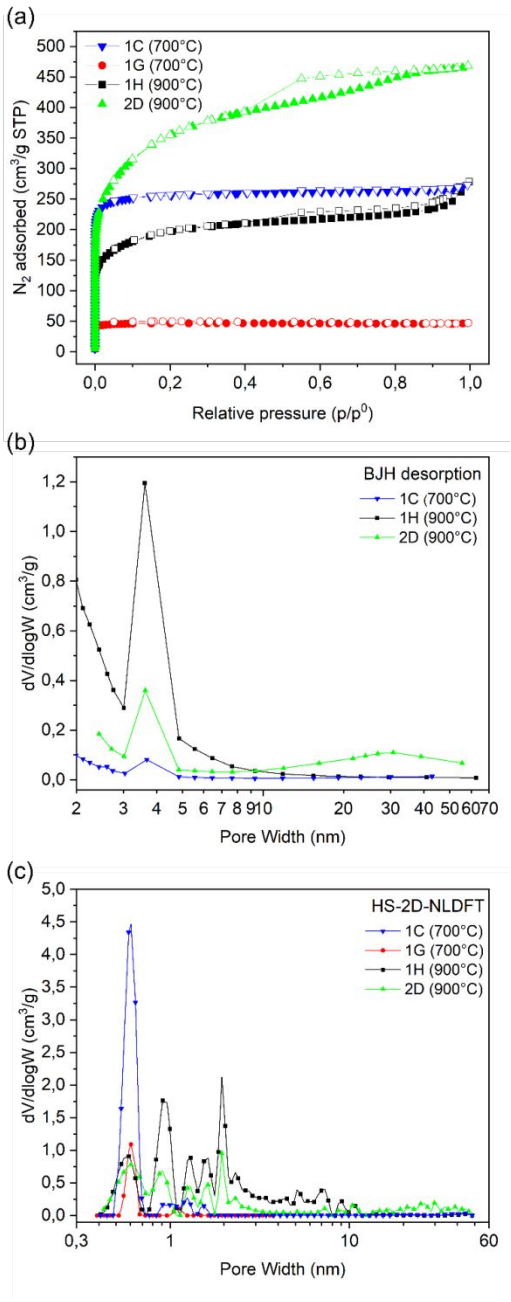

Figure 6. (a) Selected N_2 adsorption (solid symbols) and desorption (open symbols) isotherms. (b) Pore size distributions obtained using the BJH model applied to the desorption branch (the model could not be applied to sample **1G**). (c) PSD obtained using the HS-2D-NLDFT model.

The morphology of the ACs was investigated using ESEM and TEM. ESEM images (**Figure S1**) revealed the formation of holes and channels in the carbonized material, attributed to the release of volatile compounds during pyrolysis. The porosity varied with experimental conditions, such as temperature and activating agent, consistent with the previously discussed BET results. TEM micrographs (**Figure 7** and **Figure S8**) confirmed the plate-like morphology of the carbon particles and revealed microdomains with graphitic structures within a disordered carbon matrix, consistent with the Raman spectroscopy results. TEM elemental mapping images shown in **Figure 8** show that C, O, N, and P were well dispersed across the sample, with only minor variations in distribution.

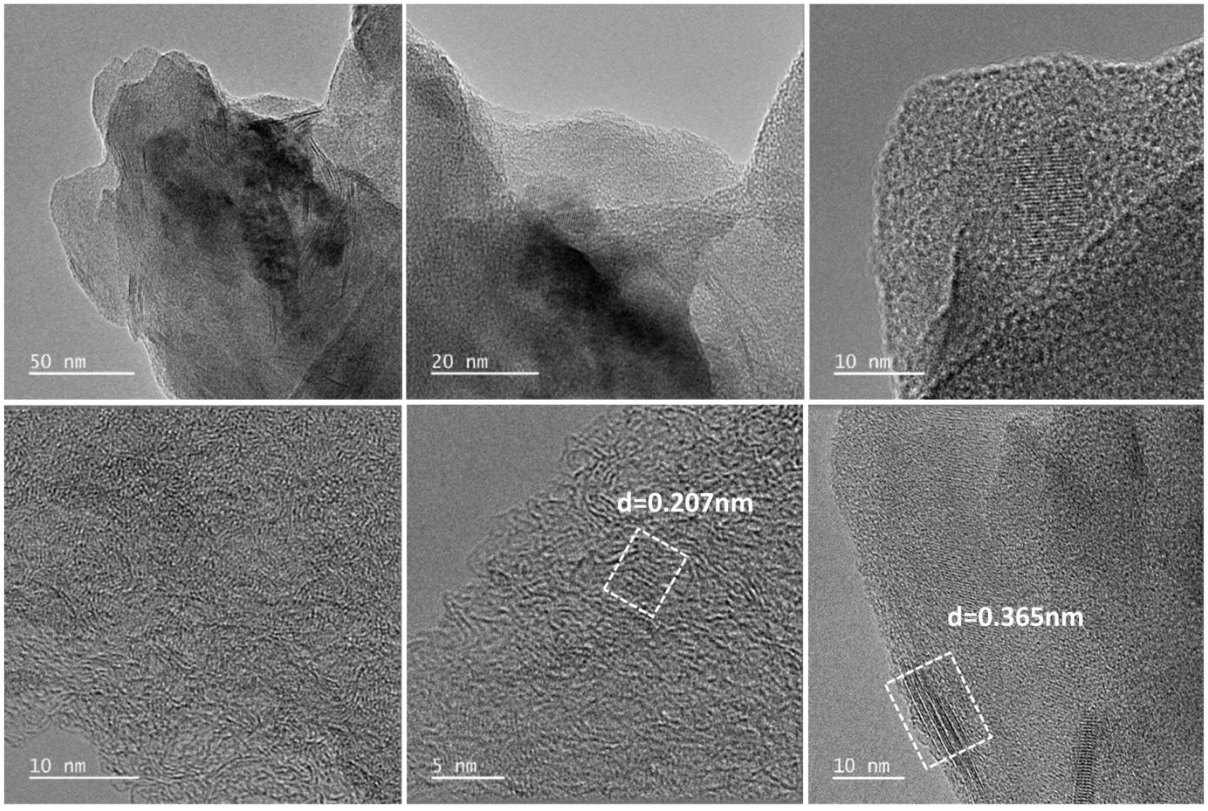

Figure 7. TEM micrographs of sample **2B** (SCG/HCCP, 900 ˚C).

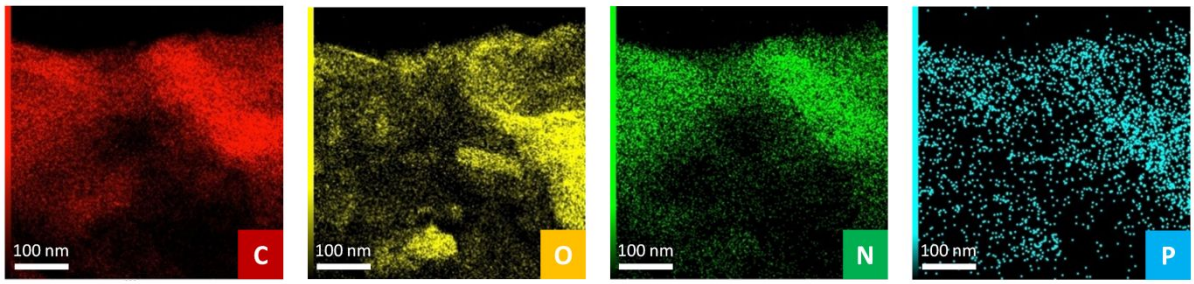

Figure 8. EDS elemental mapping of sample **2B** (SCG/HCCP, 900 ˚C).

The structure of the prepared carbons was further studied by XRD. All samples exhibited characteristic diffraction peaks at approximately 24˚, 43˚, and 80˚, corresponding to the (002), (100), and (110) graphite crystal planes, respectively (**Figure 9**). The broad width of the peaks reflects the structural disorder typical for non-graphitic carbons, while the presence of (002) diffraction indicates stacking of carbon nanosheets within disordered phase[116]. Notably, the interlayer spacing observed in the graphitic domains in TEM images (**Figure 7**) matched those calculated from the XRD data (**Table S8**).

The results from TEM, XRD, and BET analyses show that the crystalline structure of the as-prepared samples consists primarily of two types of nanosized domains: (i) turbostratic domains, which are randomly distributed and oriented throughout the material, and (ii) microporous regions, behaving like voids within the turbostratic carbon matrix[117–119]. It is also worth noting that the XRD peaks became more intense and narrower for the samples pyrolyzed at 900 ˚C compared to those at 700 ˚C, indicating increased formation of nanosized, ordered graphite-like crystallites. This structural evolution was also evident in the corresponding TEM micrographs (**Figure 7** and **Figure S8**).

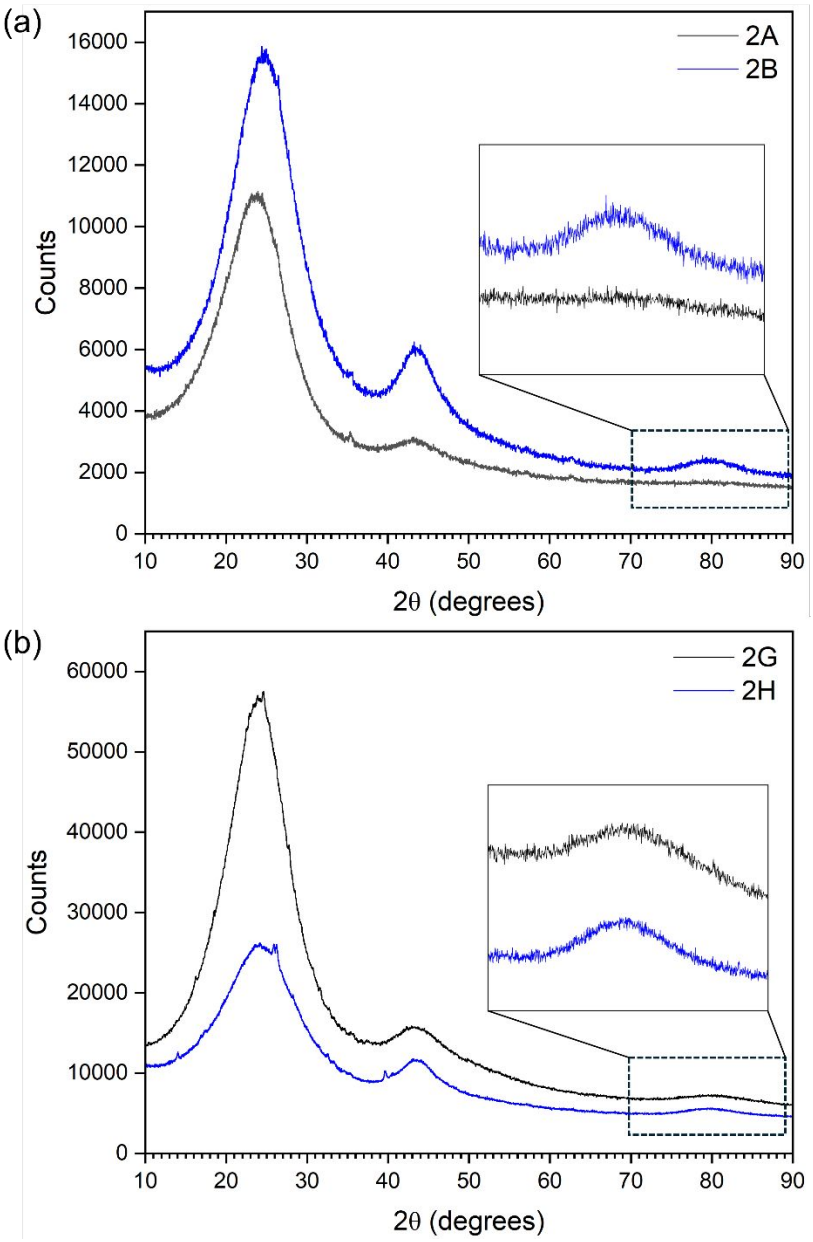

Figure 9. (a) XRD spectra of samples **2A** (SCG/HCCP, 700 ˚C) and **2B** (SCG/HCCP, 900 ˚C). (b) XRD spectra of samples **2G** (SCG/HCCP, NH_4HCO_3, 700 ˚C) and **2H** (SCG /HCCP, NH_4HCO_3, 900 ˚C).

Electrochemical Activity

The oxygen reduction reaction (ORR) is a key reaction for energy conversion technologies, including microbial fuel cells and metal–air batteries, with direct implications in environmental monitoring, wastewater treatment, and renewable energy systems. The electrocatalytic activity of selected activated carbon samples toward ORR was evaluated using cyclic voltammetry (CV) in O_2-saturated 0.1 M KOH (**Figure 10**). The results demonstrated the influence of pyrolysis temperature, N and P co-doping (introduced by HCCP during synthesis), and the use of a porosity-activating agent (NH_4HCO_3) on the electrochemical performance of SCG-derived activated carbons.

Cathodic peaks were observed in the O_2-saturated electrolyte for all prepared electrodes, whereas no peaks appeared in the N_2-saturated electrolyte, confirming electrocatalytic activity toward ORR. These peaks are attributed to the electrochemical reduction of O_2 at the catalyst surface. A positive shift in the cathodic peak potential was observed under certain synthesis conditions, indicating reduced overpotential for ORR. This shift suggests enhanced reaction kinetics, improved electron transfer, and stronger interaction with oxygen intermediates, consistent with previous reports on doped carbon-based catalysts[120,121].

For the N, P co-doped samples prepared from SCG in the presence of HCCP, the cathodic peak potential increased from 0.63 V (sample **2A**) to 0.78 V vs RHE (sample **2B**) as the pyrolysis temperature increased from 700 ˚C to 900 ˚C. The enhanced ORR activity of sample **2B** can be attributed to a higher content of graphitic nitrogen formed at elevated temperatures, which is known to improve electrical conductivity and facilitate charge transfer, in agreement with findings reported in previous studies[122–124].

The effect of the NH_4HCO_3 as a porosity-activating agent was also investigated. Its thermal decomposition can play an essential role in developing hierarchical porous structures that facilitate mass transport and provide additional active sites for ORR[125]. A small positive shift in the cathodic peak potential was observed upon NH_4HCO_3 activation: from 0.63 V to 0.67 V vs RHE for samples **2A** and **2G,** respectively (pyrolyzed at 700 ˚C), and from 0.78 V to 0.80 V vs RHE for samples **2B** and **2H**, respectively (pyrolyzed at 900 ˚C). For a more detailed analysis, samples **2G** (SCG/HCCP, pyrolyzed at 700 ˚C), **2H** (SCG/HCCP, pyrolyzed at 900 ˚C) and **1H** (SCG, pyrolyzed at 900 ˚C), all treated with NH_4HCO_3, were compared. A significant positive shift in cathodic peak potential from 0.64 V (**1H**) to 0.80 V vs RHE (**2H**) was observed, demonstrating the significant role of N and P doping, in particular, the increased P/C ratio introduced via HCCP, in enhancing ORR catalytic activity at 900 ˚C (**Table S1**). Additionally, the superior ORR performance of sample **2H** compared to **2G** (evidenced by cathodic peak potentials of 0.80 V versus 0.64 V) further confirms the synergistic effect of high-temperature pyrolysis and NH_4HCO_3 activation in promoting the formation of a mesoporous P, N co-doped graphitic structure.

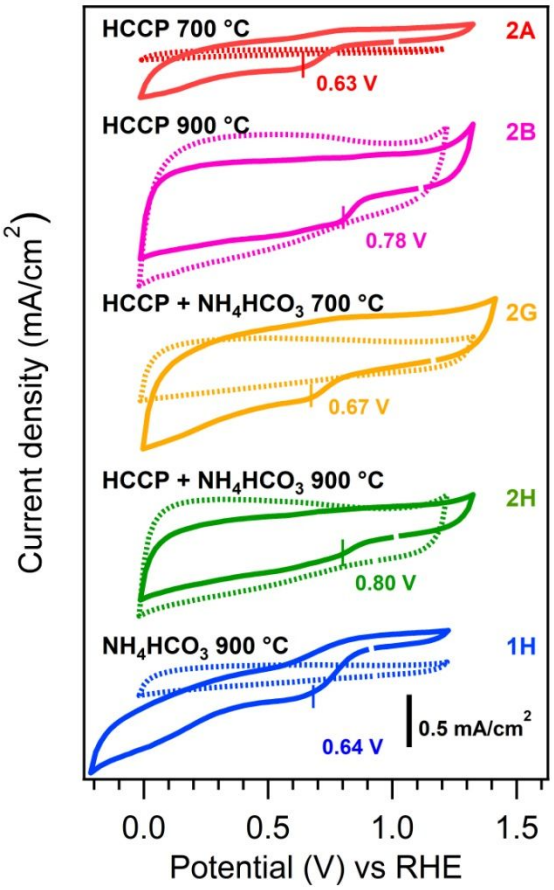

Figure 10. Cycle voltammetry (CV) curves of samples in O_2-saturated (solid lines) and N_2-saturated (dashed line) 0.1 M KOH solutions. Five consecutive scans were performed for each sample; the displayed curves correspond to the second scan, after which the response remained stable.

Conclusions

This study demonstrates that hexachlorocyclotriphosphazene (HCCP) is an effective dual source of nitrogen and phosphorus for synthesizing N, P-doped activated carbons from spent coffee grounds (SCG). NH_4HCO_3 was shown to be a promising metal-free porosity-activating agent at 900 ˚C, promoting the formation of hierarchical porous structures with a substantial mesoporous

contribution and graphitic-nitrogen-rich carbon framework. Oxalic acid also facilitated mesoporosity development at 900 ˚C, likely due to the formation of potassium oxalate from native potassium in SCG. Electrocatalytic performance toward the oxygen reduction reaction (ORR) was evaluated to assess the combined effects of pyrolysis temperature, N, P co-doping, and NH_4HCO_3 activation. The highest ORR activity was observed for the N, P co-doped sample prepared at 900 ˚C with NH_4HCO_3 activation, highlighting the synergistic roles of elevated pyrolysis temperature, enhanced dopant incorporation, and the formation of graphitic nitrogen within a hierarchical porous carbon framework. These findings underscore the potential of integrating HCCP doping and NH_4HCO_3 activation in the design of high-performance SCG-derived carbon electrocatalysts, with promising applications in waste valorization and environmental electrochemistry.

Associated content

Supporting Information. SEM images of the activated carbons, elemental and chemical composition determined by EDS and XPS, Raman spectra analysis, thermogravimetric analysis, BET data, proximate analysis, interplanar spacing calculated from XRD spectra, additional TEM images, a schematic of the three-electrode electrochemical setup, and the proposed mechanism of HCCP decomposition supported by ion-mass spectra data. This material is available free of charge via the Internet at http://pubs.acs.org.

Author information

Corresponding Authors

* Silvia Nappini; CNR - Istituto Officina dei Materiali (IOM), Area Science Park Basovizza, S.S. 14 Km 163,5, 34149 Trieste, Italy; Email: nappini@iom.cnr.it

* Roberta Bertani; Department of Industrial Engineering, UNIPD, Padova, 35131, Italy; Email: roberta.bertani@unipd.it

Present addresses:

Igor Píš; Institute of Electrical Engineering, Slovak Academy of Sciences, Bratislava, 841 04, Slovakia

Author Contributions

F.L., S.N., R.B., and E.M. contributed to the conceptualization of the study. Methodology was developed by all authors. Experimental investigation was carried out by F.L., A. di G., A.S., X.M.C.T., T.T.K.T.T., S.N., I.N.A., E.M., and I.P. The original draft was written by F.L., S.N., R.B., E.M., P.S., and I.P., and all authors participated in the review and editing of the manuscript. All authors have given approval to the final version of the manuscript.

Acknowledgements

This research received financial support by Ministero dell'Università e della Ricerca (MUR), funded by the European Union – NextGenerationEU - Project Title "NoblE metals free hierarchical Catalysts and eLectrocatalysts engIneering: in oPerando mulTi-technIque approaCh (ECLIPTIC)", ProjectNo. 2022A2A9NW-CUP: B53D2301357000, Mission 4, Component 2,

Investment 1.1), by the Department of Industrial Engineering (PROGETTO BIRD 2022), and by Italian government (Ministero dell'ambiente e della sicurezza energetica - Progetto PERMANENT - BANDO MITE PNRR Missione 2 Investimento 3.5 A - RSH2A-0O0012. The authors acknowledge Dr. D. Rossetto for TGA recording and Dr. A. Basagni for TEM analyses.

References

(1) Liu, L.; Zhang, W.; Lu, B.; Cheng, Z.; Cao, H.; Li, J.; Fan, Z.; An, X. Controllable Heteroatoms Doped Electrodes Engineered by Biomass Based Carbon for Advanced Supercapacitors: A Review. *Biomass and Bioenergy* **2024**, *186*, 107265. https://doi.org/10.1016/j.biombioe.2024.107265.

(2) Duran-Uribe, E. S.; Sepúlveda-Escribano, A.; Ramos-Fernandez, E. V. Catalytic Synergy: N,P Modification of Activated Carbon for Improved 1-Chloro-4-Nitrobenzene Reduction. *Carbon* **2024**, *227*, 119262. https://doi.org/10.1016/j.carbon.2024.119262.

(3) Bao, Y.; Liu, Y.; Wang, C.; Wang, Y.; Yuan, D.; Xu, J.; Zhu, Z.; He, Y.; Liu, J. Synergistic Removal of U(VI) from Aqueous Solution by TAC Material: Adsorption Behavior and Mechanism. *Applied Radiation and Isotopes* **2022**, *190*, 110512. https://doi.org/10.1016/j.apradiso.2022.110512.

(4) Shin, J.; Lee, Y.-G.; Lee, S.-H.; Kim, S.; Ochir, D.; Park, Y.; Kim, J.; Chon, K. Single and Competitive Adsorptions of Micropollutants Using Pristine and Alkali-Modified Biochars from Spent Coffee Grounds. *Journal of Hazardous Materials* **2020**, *400*, 123102. https://doi.org/10.1016/j.jhazmat.2020.123102.

(5) Zhang, B.; Ren, G.; Ran, L.; Liu, M.; Geng, P.; Yi, W. Green Synthesis of Biomass-Derived Porous Carbon for Electrochemical Detection of Heavy Metal Ions: Methods, Properties, and Applications. *Journal of Environmental Chemical Engineering* **2024**, *12* (5), 113903. https://doi.org/10.1016/j.jece.2024.113903.

(6) Rehman, A.; Nazir, G.; Rhee, K. Y.; Park, S.-J. Valorization of Orange Peel Waste to Tunable Heteroatom-Doped Hydrochar-Derived Microporous Carbons for Selective CO_2 Adsorption and Separation. *Science of The Total Environment* **2022**, *849*, 157805. https://doi.org/10.1016/j.scitotenv.2022.157805.

(7) Chiu, Y.-H.; Lin, L.-Y. Effect of Activating Agents for Producing Activated Carbon Using a Facile One-Step Synthesis with Waste Coffee Grounds for Symmetric Supercapacitors.

Journal of the Taiwan Institute of Chemical Engineers **2019**, *101*, 177–185. https://doi.org/10.1016/j.jtice.2019.04.050.

(8) Luo, L.; Lan, Y.; Zhang, Q.; Deng, J.; Luo, L.; Zeng, Q.; Gao, H.; Zhao, W. A Review on Biomass-Derived Activated Carbon as Electrode Materials for Energy Storage Supercapacitors. *Journal of Energy Storage* **2022**, *55*, 105839. https://doi.org/10.1016/j.est.2022.105839.

(9) Gopalakrishnan, A.; Badhulika, S. Effect of Self-Doped Heteroatoms on the Performance of Biomass-Derived Carbon for Supercapacitor Applications. *Journal of Power Sources* **2020**, *480*, 228830. https://doi.org/10.1016/j.jpowsour.2020.228830.

(10) Zhang, X.; Han, R.; Liu, Y.; Li, H.; Shi, W.; Yan, X.; Zhao, X.; Li, Y.; Liu, B. Porous and Graphitic Structure Optimization of Biomass-Based Carbon Materials from 0D to 3D for Supercapacitors: A Review. *Chemical Engineering Journal* **2023**, *460*, 141607. https://doi.org/10.1016/j.cej.2023.141607.

(11) Tan, Y.; Xu, C.; Chen, G.; Liu, Z.; Ma, M.; Xie, Q.; Zheng, N.; Yao, S. Synthesis of Ultrathin Nitrogen-Doped Graphitic Carbon Nanocages as Advanced Electrode Materials for Supercapacitor. *ACS Appl. Mater. Interfaces* **2013**, *5* (6), 2241–2248. https://doi.org/10.1021/am400001g.

(12) Abbas, Q.; Raza, R.; Shabbir, I.; Olabi, A. G. Heteroatom Doped High Porosity Carbon Nanomaterials as Electrodes for Energy Storage in Electrochemical Capacitors: A Review. *Journal of Science: Advanced Materials and Devices* **2019**, *4* (3), 341–352. https://doi.org/10.1016/j.jsamd.2019.07.007.

(13) Wang, Y.; Xu, T.; Liu, K.; Zhang, M.; Cai, X.-M.; Si, C. Biomass-Based Materials for Advanced Supercapacitor: Principles, Progress, and Perspectives. *Aggregate* **2024**, *5*(1), e428. https://doi.org/10.1002/agt2.428.

(14) Priyadharshini, M.; Pazhanivel, T.; Hariprasath, K. R. Biomass-Derived Carbon for Supercapacitors. In *Sustainable Materials for Electrochemical Capacitors*; John Wiley & Sons, Ltd, 2023; pp 427–440. https://doi.org/10.1002/9781394167104.ch18.

(15) Aziz, M. A.; Shah, S. S. Biomass-Based Supercapacitors: Design, Fabrication and Sustainability. In *Biomass-Based Supercapacitors*; John Wiley & Sons, Ltd, 2023; https://doi.org/10.1002/9781119866435.

(16) Yuan, Y.; Chen, Z.; Yu, H.; Zhang, X.; Liu, T.; Xia, M.; Zheng, R.; Shui, M.; Shu, J. Heteroatom-Doped Carbon-Based Materials for Lithium and Sodium Ion Batteries. *Energy Storage Materials* **2020**, *32*, 65–90. https://doi.org/10.1016/j.ensm.2020.07.027.

(17) Wu, F.; Li, J.; Tian, Y.; Su, Y.; Wang, J.; Yang, W.; Li, N.; Chen, S.; Bao, L. 3D Coral-like Nitrogen-Sulfur Co-Doped Carbon-Sulfur Composite for High Performance Lithium-Sulfur Batteries. *Sci Rep* **2015**, *5* (1), 13340. https://doi.org/10.1038/srep13340.

(18) Fan, W.; Zhang, H.; Wang, H.; Zhao, X.; Sun, S.; Shi, J.; Huang, M.; Liu, W.; Zheng, Y.; Li, P. Dual-Doped Hierarchical Porous Carbon Derived from Biomass for Advanced Supercapacitors and Lithium Ion Batteries. *RSC Adv.* **2019**, *9* (56), 32382–32394. https://doi.org/10.1039/C9RA06914C.

(19) Sangprasert, T.; Sattayarut, V.; Rajrujithong, C.; Khanchaitit, P.; Khemthong, P.; Chanthad, C.; Grisdanurak, N. Making Use of the Inherent Nitrogen Content of Spent Coffee Grounds to Create Nanostructured Activated Carbon for Supercapacitor and Lithium-Ion Battery Applications. *Diamond and Related Materials* **2022**, *127*, 109164. https://doi.org/10.1016/j.diamond.2022.109164.

(20) Zhou, Z.; Chen, F.; Jiang, Z.; Liu, T.; Fei, Y.; Kuang, T.; Zhong, M.; Liu, X.; Song, S. MoS_2 Nanosheets Uniformly Grown on Polyphosphazene-Derived Carbon Nanospheres for Lithium-Ion Batteries. *Surfaces and Interfaces* **2021**, *24*, 101034. https://doi.org/10.1016/j.surfin.2021.101034.

(21) Li, S.-Q.; Sun, K.; Liu, Y.-Y.; Liu, S.-L.; Zhou, J.-J.; Zhang, W.-B.; Lu, Y.-H.; Chen, X.-M.; Wang, X.-P.; Li, B.-J.; Jiang, J.-C. Coupling Co2P Nanoparticles onto N,P-Doped Biomass-Derived Carbon as Efficient Electrocatalysts for Flexible Zn–Air Batteries. *Rare Met.* **2024**, *43* (10), 4982–4991. https://doi.org/10.1007/s12598-024-02829-z.

(22) Zhang, L.; Zhou, W.; Cao, Y.; Zhang, H.; Zhu, W. N-, P-Co-Doped Hierarchically Porous Carbon Fiber Derived from Bamboo Pulp as Efficient Carbocatalyst for Reduction of 4-Nitrophenol. *Carbon Lett.* **2024**, *34* (8), 2137–2148. https://doi.org/10.1007/s42823-024-00758-6.

(23) Saka, C. Robust and Efficient Hydrogen Production Performance Using Nitrogen- and Phosphorus-Doped Microalgal Carbon-Based Metal-Free Carbon Composite. *International Journal of Hydrogen Energy* **2024**, *68*, 663–672. https://doi.org/10.1016/j.ijhydene.2024.04.286.

(24) Oh, W.-D.; Veksha, A.; Chen, X.; Adnan, R.; Lim, J.-W.; Leong, K.-H.; Lim, T.-T. Catalytically Active Nitrogen-Doped Porous Carbon Derived from Biowastes for Organics Removal via Peroxymonosulfate Activation. *Chemical Engineering Journal* **2019**, *374*, 947–957. https://doi.org/10.1016/j.cej.2019.06.001.

(25) Oh, W.-D.; Lisak, G.; Webster, R. D.; Liang, Y.-N.; Veksha, A.; Giannis, A.; Moo, J. G. S.; Lim, J.-W.; Lim, T.-T. Insights into the Thermolytic Transformation of Lignocellulosic Biomass Waste to Redox-Active Carbocatalyst: Durability of Surface Active Sites. *Applied*

Catalysis B: Environmental **2018**, *233*, 120–129. https://doi.org/10.1016/j.apcatb.2018.03.106.

(26) Lin, Y.; Wu, S.; Shi, W.; Zhang, B.; Wang, J.; Kim, Y. A.; Endo, M.; Su, D. S. Efficient and Highly Selective Boron-Doped Carbon Materials-Catalyzed Reduction of Nitroarenes. *Chem. Commun.* **2015**, *51* (66), 13086–13089. https://doi.org/10.1039/C5CC01963J.

(27) Qi, W.; Yan, P.; Su, D. S. Oxidative Dehydrogenation on Nanocarbon: Insights into the Reaction Mechanism and Kinetics via in Situ Experimental Methods. *Acc. Chem. Res.* **2018**, *51* (3), 640–648. https://doi.org/10.1021/acs.accounts.7b00475.

(28) Zuccante, G.; Acciarri, M.; Vecchio, C. L.; Gatto, I.; Baglio, V.; Pianta, N.; Ruffo, R.; Navarini, L.; Santoro, C. Oxygen Reduction Reaction Platinum Group Metal-Free Electrocatalysts Derived from Spent Coffee Grounds. *Electrochimica Acta* **2024**, *492*, 144353. https://doi.org/10.1016/j.electacta.2024.144353.

(29) Ren, G.; Huang, B.; Li, C.; Lin, C.; Qian, Y. Facile and Template-Free Strategy to Construct N, P Co-Doped Porous Carbon Nanosheets as a Highly Efficient Electrocatalyst towards Oxygen Reduction Reaction. *Journal of Electroanalytical Chemistry* **2020**, *877*, 114732. https://doi.org/10.1016/j.jelechem.2020.114732.

(30) Choi, C. H.; Park, S. H.; Woo, S. I. Binary and Ternary Doping of Nitrogen, Boron, and Phosphorus into Carbon for Enhancing Electrochemical Oxygen Reduction Activity. *ACS Nano* **2012**, *6* (8), 7084–7091. https://doi.org/10.1021/nn3021234.

(31) Wang, K.; Wang, H.; Ji, S.; Feng, H.; Linkov, V.; Wang, R. Biomass-Derived Activated Carbon as High-Performance Non-Precious Electrocatalyst for Oxygen Reduction. *RSC Adv.* **2013**, *3* (30), 12039–12042. https://doi.org/10.1039/C3RA41978A.

(32) Lv, K.; Zhang, H.; Chen, S. Nitrogen and Phosphorus Co-Doped Carbon Modified Activated Carbon as an Efficient Oxygen Reduction Catalyst for Microbial Fuel Cells. *RSC Adv.* **2018**, *8* (2), 848–855. https://doi.org/10.1039/C7RA12907F.

(33) Zhao, Z.; Wang, Y.; Li, M.; Yang, R. High Performance N-Doped Porous Activated Carbon Based on Chicken Feather for Supercapacitors and CO2 Capture. *RSC Adv.* **2015**, *5* (44), 34803–34811. https://doi.org/10.1039/C5RA01569C.

(34) Li, K.; Chen, W.; Yang, H.; Chen, Y.; Xia, S.; Xia, M.; Tu, X.; Chen, H. Mechanism of Biomass Activation and Ammonia Modification for Nitrogen-Doped Porous Carbon Materials. *Bioresource Technology* **2019**, *280*, 260–268. https://doi.org/10.1016/j.biortech.2019.02.039.

(35) He, J.; Zhang, D.; Han, M.; Liu, X.; Wang, Y.; Li, Y.; Zhang, X.; Wang, K.; Feng, H.; Wang, Y. One-Step Large-Scale Fabrication of Nitrogen Doped Microporous Carbon by Self-

Activation of Biomass for Supercapacitors Application. *Journal of Energy Storage* **2019**, *21*, 94–104. https://doi.org/10.1016/j.est.2018.11.015.

(36) Gao, R.; Pan, L.; Lu, J.; Xu, J.; Zhang, X.; Wang, L.; Zou, J.-J. Phosphorus-Doped and Lattice-Defective Carbon as Metal-like Catalyst for the Selective Hydrogenation of Nitroarenes. *ChemCatChem* **2017**, *9* (22), 4287–4294. https://doi.org/10.1002/cctc.201700904.

(37) Yuan, L.-P.; Wu, Z.-Y.; Jiang, W.-J.; Tang, T.; Niu, S.; Hu, J.-S. Phosphorus-Doping Activates Carbon Nanotubes for Efficient Electroreduction of Nitrogen to Ammonia. *Nano Res.* **2020**, *13* (5), 1376–1382. https://doi.org/10.1007/s12274-020-2637-8.

(38) Chen, B.; Wu, W.; Li, C.; Wang, Y.; Zhang, Y.; Fu, L.; Zhu, Y.; Zhang, L.; Wu, Y. Oxygen/Phosphorus Co-Doped Porous Carbon from Cicada Slough as High-Performance Electrode Material for Supercapacitors. *Sci Rep* **2019**, *9* (1), 5431. https://doi.org/10.1038/s41598-019-41769-y.

(39) Puziy, A. M.; Poddubnaya, O. I.; Gawdzik, B.; Tascón, J. M. D. Phosphorus-Containing Carbons: Preparation, Properties and Utilization. *Carbon* **2020**, *157*, 796–846. https://doi.org/10.1016/j.carbon.2019.10.018.

(40) Ma, W.; Xie, L.; Dai, L.; Sun, G.; Chen, J.; Su, F.; Cao, Y.; Lei, H.; Kong, Q.; Chen, C.-M. Influence of Phosphorus Doping on Surface Chemistry and Capacitive Behaviors of Porous Carbon Electrode. *Electrochimica Acta* **2018**, *266*, 420–430. https://doi.org/10.1016/j.electacta.2018.02.031.

(41) Huang, C.; Sun, T.; Hulicova-Jurcakova, D. Wide Electrochemical Window of Supercapacitors from Coffee Bean-Derived Phosphorus-Rich Carbons. *ChemSusChem* **2013**, *6* (12), 2330–2339. https://doi.org/10.1002/cssc.201300457.

(42) Wang, F.; Hu, C.; Lian, J.; Zhou, M.; Wang, K.; Yan, J.; Jiang, K. Phosphorus-Doped Activated Carbon as a Promising Additive for High Performance Lead Carbon Batteries. *RSC Adv.* **2017**, *7* (7), 4174–4178. https://doi.org/10.1039/C6RA26093D.

(43) Yang, W.; Yang, W.; Kong, L.; Song, A.; Qin, X.; Shao, G. Phosphorus-Doped 3D Hierarchical Porous Carbon for High-Performance Supercapacitors: A Balanced Strategy for Pore Structure and Chemical Composition. *Carbon* **2018**, *127*, 557–567. https://doi.org/10.1016/j.carbon.2017.11.050.

(44) Blankenship, L. S.; Balahmar, N.; Mokaya, R. Oxygen-Rich Microporous Carbons with Exceptional Hydrogen Storage Capacity. *Nat Commun* **2017**, *8* (1), 1545. https://doi.org/10.1038/s41467-017-01633-x.

(45) Guo, D.; Song, X.; Li, B.; Tan, L.; Ma, H.; Pang, H.; Wang, X.; Zhang, L.; Chu, D. Oxygen Enriched Carbon with Hierarchical Porous Structure Derived from Biomass Waste for High-Performance Symmetric Supercapacitor with Decent Specific Capacity. *Journal of Electroanalytical Chemistry* **2019**, *855*, 113349. https://doi.org/10.1016/j.jelechem.2019.113349.

(46) Zhao, Y.; Ran, W.; He, J.; Song, Y.; Zhang, C.; Xiong, D.-B.; Gao, F.; Wu, J.; Xia, Y. Oxygen-Rich Hierarchical Porous Carbon Derived from Artemia Cyst Shells with Superior Electrochemical Performance. *ACS Appl. Mater. Interfaces* **2015**, *7* (2), 1132–1139. https://doi.org/10.1021/am506815f.

(47) Wang, C.; Wu, D.; Wang, H.; Gao, Z.; Xu, F.; Jiang, K. A Green and Scalable Route to Yield Porous Carbon Sheets from Biomass for Supercapacitors with High Capacity. *J. Mater. Chem. A* **2018**, *6* (3), 1244–1254. https://doi.org/10.1039/C7TA07579K.

(48) Mishra, R.; Panda, P.; Barman, S. Synthesis of Sulfur-Doped Porous Carbon for Supercapacitor and Gas Adsorption Applications. *International Journal of Energy Research* **2022**, *46* (3), 2585–2600. https://doi.org/10.1002/er.7330.

(49) Wang, D.; Wang, S.; Lu, Z. S-Doped 3D Porous Carbons Derived from Potassium Thioacetate Activation Strategy for Zinc-Ion Hybrid Supercapacitor Applications. *International Journal of Energy Research* **2021**, *45* (2), 2498–2510. https://doi.org/10.1002/er.5944.

(50) Yaglikci, S.; Gokce, Y.; Yagmur, E.; Aktas, Z. The Performance of Sulphur Doped Activated Carbon Supercapacitors Prepared from Waste Tea. *Environmental Technology* **2020**, *41* (1), 36–48. https://doi.org/10.1080/09593330.2019.1575480.

(51) Tian, J.; Zhang, H.; Liu, Z.; Qin, G.; Li, Z. One-Step Synthesis of 3D Sulfur-Doped Porous Carbon with Multilevel Pore Structure for High-Rate Supercapacitors. *International Journal of Hydrogen Energy* **2018**, *43* (3), 1596–1605. https://doi.org/10.1016/j.ijhydene.2017.11.091.

(52) Miyashita, K.; Kondo, T.; Sugai, S.; Tei, T.; Nishikawa, M.; Tojo, T.; Yuasa, M. Boron-Doped Nanodiamond as an Electrode Material for Aqueous Electric Double-Layer Capacitors. *Sci Rep* **2019**, *9* (1), 17846. https://doi.org/10.1038/s41598-019-54197-9.

(53) Liu, S.; Xu, J.; Zhou, H.; Wang, J.; Meng, X. B-Doped Si@C Nanorod Anodes for High-Performance Lithium-Ion Batteries. *Journal of Nanomaterials* **2019**, *2019* (1), 6487156. https://doi.org/10.1155/2019/6487156.

(54) Gao, J.; Wang, X.; Zhang, Y.; Liu, J.; Lu, Q.; Liu, M. Boron-Doped Ordered Mesoporous Carbons for the Application of Supercapacitors. *Electrochimica Acta* **2016**, *207*, 266–274. https://doi.org/10.1016/j.electacta.2016.05.013.

(55) Liu, B.; Guo, W.; Wang, H.; Si, Q.; Zhao, Q.; Luo, H.; Ren, N. B-Doped Graphitic Porous Biochar with Enhanced Surface Affinity and Electron Transfer for Efficient Peroxydisulfate Activation. *Chemical Engineering Journal* **2020**, *396*, 125119. https://doi.org/10.1016/j.cej.2020.125119.

(56) Srivastava, S.; Jain, S. K.; Gupta, G.; Senguttuvan, T. D.; Gupta, B. K. Boron-Doped Few-Layer Graphene Nanosheet Gas Sensor for Enhanced Ammonia Sensing at Room Temperature. *RSC Adv.* **2020**, *10* (2), 1007–1014. https://doi.org/10.1039/C9RA08707A.

(57) Bleu, Y.; Bourquard, F.; Barnier, V.; Lefkir, Y.; Reynaud, S.; Loir, A.-S.; Garrelie, F.; Donnet, C. Boron-Doped Graphene Synthesis by Pulsed Laser Co-Deposition of Carbon and Boron. *Applied Surface Science* **2020**, *513*, 145843. https://doi.org/10.1016/j.apsusc.2020.145843.

(58) Preuss, K.; Siwoniku, A. M.; Bucur, C. I.; Titirici, M.-M. The Influence of Heteroatom Dopants Nitrogen, Boron, Sulfur, and Phosphorus on Carbon Electrocatalysts for the Oxygen Reduction Reaction. *ChemPlusChem* **2019**, *84* (5), 457–464. https://doi.org/10.1002/cplu.201900083.

(59) Wang, J.; Shen, L.; Xu, Y.; Dou, H.; Zhang, X. Lamellar-Structured Biomass-Derived Phosphorus- and Nitrogen-Co-Doped Porous Carbon for High-Performance Supercapacitors. *New J. Chem.* **2015**, *39* (12), 9497–9503. https://doi.org/10.1039/C5NJ02080H.

(60) Luyen Doan, T. L.; Tran, D. T.; Nguyen, D. C.; Tuan Le, H.; Kim, N. H.; Lee, J. H. Hierarchical Three-Dimensional Framework Interface Assembled from Oxygen-Doped Cobalt Phosphide Layer-Shelled Metal Nanowires for Efficient Electrocatalytic Water Splitting. *Applied Catalysis B: Environmental* **2020**, *261*, 118268. https://doi.org/10.1016/j.apcatb.2019.118268.

(61) Yang, I.; Yoo, J.; Kwon, D.; Choi, D.; Kim, M.-S.; Jung, J. C. Improvement of a Commercial Activated Carbon for Organic Electric Double-Layer Capacitors Using a Consecutive Doping Method. *Carbon* **2020**, *160*, 45–53. https://doi.org/10.1016/j.carbon.2020.01.024.

(62) Wang, Y.; Qu, Q.; Gao, S.; Tang, G.; Liu, K.; He, S.; Huang, C. Biomass Derived Carbon as Binder-Free Electrode Materials for Supercapacitors. *Carbon* **2019**, *155*, 706–726. https://doi.org/10.1016/j.carbon.2019.09.018.

(63) Wang, Q.; Yan, J.; Fan, Z. Carbon Materials for High Volumetric Performance Supercapacitors: Design, Progress, Challenges and Opportunities. *Energy Environ. Sci.* **2016**, *9* (3), 729–762. https://doi.org/10.1039/C5EE03109E.

(64) Dagdag, O.; Kim, H.; Dagdag, O.; Kim, H. Progress in the Field of Cyclophosphazenes: Preparation, Properties, and Applications. *Polymers* **2023**, *16* (1). https://doi.org/10.3390/polym16010122.

(65) Rothemund, S.; Teasdale, I. Preparation of Polyphosphazenes: A Tutorial Review. *Chem. Soc. Rev.* **2016**, *45* (19), 5200–5215. https://doi.org/10.1039/C6CS00340K.

(66) Liu, W.; Zhang, S.; Dar, S. U.; Zhao, Y.; Akram, R.; Zhang, X.; Jin, S.; Wu, Z.; Wu, D. Polyphosphazene-Derived Heteroatoms-Doped Carbon Materials for Supercapacitor Electrodes. *Carbon* **2018**, *129*, 420–427. https://doi.org/10.1016/j.carbon.2017.12.016.

(67) Yang, F.; Zhang, S.; Yang, Y.; Liu, W.; Qiu, M.; Abbas, Y.; Wu, Z.; Wu, D. Heteroatoms Doped Carbons Derived from Crosslinked Polyphosphazenes for Supercapacitor Electrodes. *Electrochimica Acta* **2019**, *328*, 135064. https://doi.org/10.1016/j.electacta.2019.135064.

(68) Yang, F.; Qiu, M.; Miao, Z.; Zhang, T.; Zhang, S.; Wu, Z. N, P-Codoped Carbon Film Derived from Phosphazenes and Its Printing Integration with a Polymer Carpet Via "Molecular Welding" for Flexible Electronics. *ACS Appl. Mater. Interfaces* **2021**, *13* (25), 29894–29905. https://doi.org/10.1021/acsami.1c04010.

(69) Qiu, M.; Zhang, S.; Li, M.; Abbas, Y.; Yang, F.; Miao, Z.; Liu, W.; Qi, S.; Wu, Z. Tetra-Heteroatom-Doped Ultra-Mesoporous Carbon from Polyphosphazene for High-Performance Supercapacitors. *ChemElectroChem* **2021**, *8* (12), 2205–2213. https://doi.org/10.1002/celc.202100421.

(70) Li, X.; Lv, Z.; Wu, M.; Li, X.; Li, Z. N, P Co-Doped Porous Carbon from Cross-Linking Cyclophosphazene for High-Performance Supercapacitors. *Journal of Electroanalytical Chemistry* **2021**, *881*, 114952. https://doi.org/10.1016/j.jelechem.2020.114952.

(71) Qiu, M.; Zhang, S.; Abbas, Y.; Zhang, C.; Liu, W.; Wu, Z.; Dai, S.; Zhang, T. Heteroatom-Doped Ultrahigh Specific Area Carbons from Hybrid Polymers with Promising Capacitive Performance. *Journal of Power Sources* **2020**, *478*, 228761. https://doi.org/10.1016/j.jpowsour.2020.228761.

(72) Wu, P.; Yu, S.; Liu, H.; Zhang, X.; Hou, L.; Liu, S.; Fu, J. Lanthanum Ion Modification of Aminated Cyclomatrix Polyphosphazene-Coated Porous Carbon Nanosheets for Rapid, Efficient and Selective Removal of Phosphate. *Applied Surface Science* **2022**, *593*, 153359. https://doi.org/10.1016/j.apsusc.2022.153359.

(73) Liu, X.; Liu, Y.; Wang, Y.; Yuan, D.; Liu, J.; Chew, J. W. Preparation of Porous Carbon Materials by Polyphosphazene as Precursor for Sorption of U(VI). *Colloid and Interface Science Communications* **2021**, *41*, 100387. https://doi.org/10.1016/j.colcom.2021.100387.

(74) Wang, M.; Xu, Z.; Fu, J.; Du, H.; Wang, S. Effect of Chemical Activators on Polyphosphazene-Based Hierarchical Porous Carbons and Their Good CO_2 Capture. *Diamond and Related Materials* **2022**, *125*, 108966. https://doi.org/10.1016/j.diamond.2022.108966.

(75) Jiang, J.; Chen, H.; Wang, Z.; Bao, L.; Qiang, Y.; Guan, S.; Chen, J. Nitrogen-Doped Hierarchical Porous Carbon Microsphere through KOH Activation for Supercapacitors. *Journal of Colloid and Interface Science* **2015**, *452*, 54–61. https://doi.org/10.1016/j.jcis.2015.04.012.

(76) Zou, W.; Zhang, S.; Ali, Z.; Miao, Z.; Abbas, Y.; Liu, W.; Qiu, M.; Wu, Z. Structure Control of Heteroatoms' Self-Doped Porous Carbon Materials Derived from Cyclomatrix Polyphosphazene for High-Performance Supercapacitor Application. *Ionics* **2022**, *28* (8), 3985–3999. https://doi.org/10.1007/s11581-022-04601-8.

(77) Dar, S. U.; Ud Din, M. A.; Hameed, M. U.; Ali, S.; Akram, R.; Wu, Z.; Wu, D. Oxygen Reduction Reaction of (C-PCTNB@CNTs): A Nitrogen and Phosphorus Dual-Doped Carbon Electro-Catalyst Derived from Polyphosphazenes. *Journal of Power Sources* **2018**, *373*, 61–69. https://doi.org/10.1016/j.jpowsour.2017.11.006.

(78) Wei, X.; Zheng, D.; Zhao, M.; Chen, H.; Fan, X.; Gao, B.; Gu, L.; Guo, Y.; Qin, J.; Wei, J.; Zhao, Y.; Zhang, G. Cross-Linked Polyphosphazene Hollow Nanosphere-Derived N/P-Doped Porous Carbon with Single Nonprecious Metal Atoms for the Oxygen Reduction Reaction. *Angewandte Chemie* **2020**, *132* (34), 14747–14754. https://doi.org/10.1002/ange.202006175.

(79) Zhou, Y.; Huang, Q.; Low, C. T. J.; Walton, R. I.; McNally, T.; Wan, C. Heteroatom-Doped Core/Shell Carbonaceous Framework Materials: Synthesis, Characterization and Electrochemical Properties. *New J. Chem.* **2019**, *43* (14), 5632–5641. https://doi.org/10.1039/C8NJ05193C.

(80) Ali, Z.; Mushtaq, M. A.; Abbas, Y.; Liu, W.; Wu, Z. Inorganic Nanocrystal-Carbon Composite Derived from Cross-Linked Gallic Acid Derivative of Polyphosphazenes for the Efficient Oxygen Evolution Reaction. *Carbon Lett.* **2023**, *33* (3), 737–749. https://doi.org/10.1007/s42823-022-00455-2.

(81) Ali, Z.; Zaman, F.; Basharat, M.; Liu, W.; Zhang, T.; Wu, Z. Heteroatom Ternary-Doped Porous Carbons Derived from Poly (Cyclotriphosphazene-Co-4,4-Aminophenylether) Microspheres as Electrodes for Supercapacitors. *J Solid State Electrochem* **2023**, *27* (3), 627–640. https://doi.org/10.1007/s10008-022-05349-x.

(82) Abbas, Y.; Basharat, M.; Liu, W.; Khan, M. S.; Zhang, S.; Ali, S.; Wu, Z.; Wu, D. Substantial Role of Nitrogen and Sulfur in Quaternary-Atom-Doped Multishelled Carbon

Nanospheres for the Oxygen Evolution Reaction. *ACS Sustainable Chem. Eng.* **2020**, *8* (10), 4284–4291. https://doi.org/10.1021/acssuschemeng.0c00592.

(83) Abbas, Y.; Ali, S.; Basharat, M.; Zou, W.; Yang, F.; Liu, W.; Zhang, S.; Wu, Z.; Akhtar, N.; Wu, D. Heteroatom-Doped Carbon Nanoparticle–Ionic Liquid Composites as Electrochemical Sensors for Uric Acid. *ACS Appl. Nano Mater.* **2020**, *3* (11), 11383–11390. https://doi.org/10.1021/acsanm.0c02466.

(84) Ren, G.; Li, Y.; Chen, Q.; Qian, Y.; Zheng, J.; Zhu, Y.; Teng, C. Sepia-Derived N, P Co-Doped Porous Carbon Spheres as Oxygen Reduction Reaction Electrocatalyst and Supercapacitor. *ACS Sustainable Chem. Eng.* **2018**, *6* (12), 16032–16038. https://doi.org/10.1021/acssuschemeng.8b02170.

(85) Rosson, E.; Sgarbossa, P.; Mozzon, M.; Venturino, F.; Bogialli, S.; Glisenti, A.; Talon, A.; Moretti, E.; Carturan, S. M.; Tamburini, S.; Famengo, A.; da Costa Ribeiro, A. P.; Benhabiles, S.; Kamel, R.; Zorzi, F.; Bertani, R. Novel Correlations between Spectroscopic and Morphological Properties of Activated Carbons from Waste Coffee Grounds. *Processes* **2021**, *9* (9), 1637. https://doi.org/10.3390/pr9091637.

(86) Qiu, M.; Fu, X.; Yang, F.; Qi, S.; Wu, Z.; Zhong, W.-H. In-Situ Synthesis of N, O, P-Doped Hierarchical Porous Carbon from Poly-Bis(Phenoxy)Phosphazene for Polysulfide-Trapping Interlayer in Lithium-Sulfur Batteries. *Chemistry – A European Journal* **2021**, *27* (38), 9876–9884. https://doi.org/10.1002/chem.202100693.

(87) Ren, G.; Chen, S.; Zhang, J.; Zhang, N.; Jiao, C.; Qiu, H.; Liu, C.; Wang, H.-L. N-Doped Porous Carbon Spheres as Metal-Free Electrocatalyst for Oxygen Reduction Reaction. *J. Mater. Chem. A* **2021**, *9* (9), 5751–5758. https://doi.org/10.1039/D0TA11493F.

(88) Khalil, K. M. S.; Elhamdy, W. A.; Elsamahy, A. A. Biomass Derived P−doped Activated Carbon as Nanostructured Mesoporous Adsorbent for Chromium(VI) Pollutants with Pronounced Functional Efficiency and Recyclability. *Colloids and Surfaces A: Physicochemical and Engineering Aspects* **2022**, *641*, 128553. https://doi.org/10.1016/j.colsurfa.2022.128553.

(89) Puziy, A. M.; Poddubnaya, O. I.; Socha, R. P.; Gurgul, J.; Wisniewski, M. XPS and NMR Studies of Phosphoric Acid Activated Carbons. *Carbon* **2008**, *46* (15), 2113–2123. https://doi.org/10.1016/j.carbon.2008.09.010.

(90) Morgan, D. J. Comments on the XPS Analysis of Carbon Materials. *C* **2021**, *7* (3). https://doi.org/10.3390/c7030051.

(91) Ganguly, A.; Sharma, S.; Papakonstantinou, P.; Hamilton, J. Probing the Thermal Deoxygenation of Graphene Oxide Using High-Resolution In Situ X-Ray-Based

Spectroscopies. *J. Phys. Chem. C* **2011**, *115* (34), 17009–17019. https://doi.org/10.1021/jp203741y.

(92) Khalil, K. M. S.; Elhamdy, W. A.; Mohammed, K. M. H.; Said, A. E.-A. A. Nanostructured P-Doped Activated Carbon with Improved Mesoporous Texture Derived from Biomass for Enhanced Adsorption of Industrial Cationic Dye Contaminants. *Materials Chemistry and Physics* **2022**, *282*, 125881. https://doi.org/10.1016/j.matchemphys.2022.125881.

(93) Beyssac, O.; Goffé, B.; Petitet, J.-P.; Froigneux, E.; Moreau, M.; Rouzaud, J.-N. On the Characterization of Disordered and Heterogeneous Carbonaceous Materials by Raman Spectroscopy. *Spectrochimica Acta Part A: Molecular and Biomolecular Spectroscopy* **2003**, *59* (10), 2267–2276. https://doi.org/10.1016/S1386-1425(03)00070-2.

(94) Umeda, H.; Enami, M. Testing for Robustness on Estimation of Graphitization Degree by Raman Spectroscopy. *Journal of Mineralogical and Petrological Sciences* **2014**, *109* (6), 279–285. https://doi.org/10.2465/jmps.131211.

(95) Ferrari, A. C. Raman Spectroscopy of Graphene and Graphite: Disorder, Electron–Phonon Coupling, Doping and Nonadiabatic Effects. *Solid State Communications* **2007**, *143* (1), 47–57. https://doi.org/10.1016/j.ssc.2007.03.052.

(96) Gao, Y.; Zou, C.; She, Y.; Huang, Z.; Li, S. Analysis of Structural Heterogeneity in Low-Rank Coal and Its Pyrolyzed Char Using Multi-Point Scanning Micro-Raman Spectroscopy. *Molecules* **2024**, *29* (10), 2361. https://doi.org/10.3390/molecules29102361.

(97) Matei Ghimbeu, C.; Zhang, B.; Martinez de Yuso, A.; Réty, B.; Tarascon, J.-M. Valorizing Low Cost and Renewable Lignin as Hard Carbon for Na-Ion Batteries: Impact of Lignin Grade. *Carbon* **2019**, *153*, 634–647. https://doi.org/10.1016/j.carbon.2019.07.026.

(98) Grimm, A.; dos Reis, G. S.; Khokarale, S. G.; Ekman, S.; Lima, E. C.; Xiong, S.; Hultberg, M. Shiitake Spent Mushroom Substrate as a Sustainable Feedstock for Developing Highly Efficient Nitrogen-Doped Biochars for Treatment of Dye-Contaminated Water. *Journal of Water Process Engineering* **2023**, *56*, 104435. https://doi.org/10.1016/j.jwpe.2023.104435.

(99) Dou, X.; Hasa, I.; Saurel, D.; Vaalma, C.; Wu, L.; Buchholz, D.; Bresser, D.; Komaba, S.; Passerini, S. Hard Carbons for Sodium-Ion Batteries: Structure, Analysis, Sustainability, and Electrochemistry. *Materials Today* **2019**, *23*, 87–104. https://doi.org/10.1016/j.mattod.2018.12.040.

(100) Merlen, A.; Buijnsters, J. G.; Pardanaud, C. A Guide to and Review of the Use of Multiwavelength Raman Spectroscopy for Characterizing Defective Aromatic Carbon Solids: From Graphene to Amorphous Carbons. *Coatings* **2017**, *7* (10), 153. https://doi.org/10.3390/coatings7100153.

(101) Hosseinzadeh, J.; Mahdavi, S.; Ashori, A.; Spitsyn, A. Synthesis and Characterization of Hierarchically Porous Carbon Anodes from Furfural Biorefinery Residues for Sustainable Lithium-Ion Batteries. *Journal of Analytical and Applied Pyrolysis* **2024**, *182*, 106691. https://doi.org/10.1016/j.jaap.2024.106691.

(102) Liu, Y.; Li, K.; Liu, Y.; Pu, L.; Chen, Z.; Deng, S. The High-Performance and Mechanism of P-Doped Activated Carbon as a Catalyst for Air-Cathode Microbial Fuel Cells. *J. Mater. Chem. A* **2015**, *3* (42), 21149–21158. https://doi.org/10.1039/C5TA04595A.

(103) Cançado, L. G.; Jorio, A.; Ferreira, E. H. M.; Stavale, F.; Achete, C. A.; Capaz, R. B.; Moutinho, M. V. O.; Lombardo, A.; Kulmala, T. S.; Ferrari, A. C. Quantifying Defects in Graphene via Raman Spectroscopy at Different Excitation Energies. *Nano Lett.* **2011**, *11* (8), 3190–3196. https://doi.org/10.1021/nl201432g.

(104) Lazzarini, A.; Piovano, A.; Pellegrini, R.; Leofanti, G.; Agostini, G.; Rudić, S.; Chierotti, M. R.; Gobetto, R.; Battiato, A.; Spoto, G.; Zecchina, A.; Lamberti, C.; Groppo, E. A Comprehensive Approach to Investigate the Structural and Surface Properties of Activated Carbons and Related Pd-Based Catalysts. *Catal. Sci. Technol.* **2016**, *6* (13), 4910–4922. https://doi.org/10.1039/C6CY00159A.

(105) Maruthapandi, M.; Gedanken, A. A Short Report on the Polymerization of Pyrrole and Its Copolymers by Sonochemical Synthesis of Fluorescent Carbon Dots. *Polymers* **2019**, *11* (8), 1240. https://doi.org/10.3390/polym11081240.

(106) Strelko Jr, V.; Streat, M.; Kozynchenko, O. Preparation, Characterisation and Sorptive Properties of Polymer Based Phosphorus-Containing Carbon. *Reactive and Functional Polymers* **1999**, *41* (1), 245–253. https://doi.org/10.1016/S1381-5148(99)00061-9.

(107) Sannigrahi, P.; Ingall, E. Polyphosphates as a Source of Enhanced P Fluxes in Marine Sediments Overlain by Anoxic Waters: Evidence from 31P NMR. *Geochem Trans* **2005**, *6* (3), 52. https://doi.org/10.1186/1467-4866-6-52.

(108) Men'shchikov, I. E.; Shiryaev, A. A.; Shkolin, A. V.; Grinchenko, A. E.; Khozina, E. V.; Averin, A. A.; Fomkin, A. A. One-Stage Synthesis of Microporous Carbon Adsorbents from Walnut Shells—Evolution of Porosity and Structure. *C* **2024**, *10* (3), 79. https://doi.org/10.3390/c10030079.

(109) Sinha, P.; Datar, A.; Jeong, C.; Deng, X.; Chung, Y. G.; Lin, L.-C. Surface Area Determination of Porous Materials Using the Brunauer–Emmett–Teller (BET) Method: Limitations and Improvements. *J. Phys. Chem. C* **2019**, *123* (33), 20195–20209. https://doi.org/10.1021/acs.jpcc.9b02116.

(110) Dai, Z.; Ren, P.-G.; Zhang, H.; Gao, X.; Jin, Y.-L. Nitrogen-Doped and Hierarchically Porous Carbon Derived from Spent Coffee Ground for Efficient Adsorption of Organic Dyes. *Carbon Lett.* **2021**, *31* (6), 1249–1260. https://doi.org/10.1007/s42823-021-00248-z.

(111) Wang, C.-H.; Wen, W.-C.; Hsu, H.-C.; Yao, B.-Y. High-Capacitance KOH-Activated Nitrogen-Containing Porous Carbon Material from Waste Coffee Grounds in Supercapacitor. *Advanced Powder Technology* **2016**, *27* (4), 1387–1395. https://doi.org/10.1016/j.apt.2016.04.033.

(112) Huang, Y.; Zang, Y.; Ruan, S.; Zhang, Y.; Gao, P.; Yin, W.; Hou, C.; Huo, D.; Yang, M.; Fa, H. A High Efficiency N, P Doped Porous Carbon Nanoparticles Derived from Lotus Leaves for Simultaneous Electrochemical Determination of Ascorbic Acid, Dopamine, and Uric Acid. *Microchemical Journal* **2021**, *165*, 106152. https://doi.org/10.1016/j.microc.2021.106152.

(113) Yang, X.; Wang, X.; Yu, X.; Ye, X.; Lu, B.; Huang, B.; Lin, G. In-Situ N, P Co-Doped Porous Carbon Derived from Biomass Waste for Supercapacitors. *Journal of Electroanalytical Chemistry* **2024**, *972*, 118646. https://doi.org/10.1016/j.jelechem.2024.118646.

(114) Dobele, G.; Volperts, A.; Plavniece, A.; Zhurinsh, A.; Upskuviene, D.; Balciunaite, A.; Niaura, G.; Colmenares-Rausseo, L. C.; Tamasauskaite-Tamasiunaite, L.; Norkus, E. Thermochemical Activation of Wood with NaOH, KOH and H_3PO_4 for the Synthesis of Nitrogen-Doped Nanoporous Carbon for Oxygen Reduction Reaction. *Molecules* **2024**, *29* (10), 2238. https://doi.org/10.3390/molecules29102238.

(115) Lazarević-Pašti, T.; Anićijević, V.; Karkalić, R.; Baljozović, M.; Babić, B.; Pašti, I. A. Nitrogen-Doped Carbon Cryogels as Adsorbents: Efficient Removal of Organophosphate Pesticides from Water and Assessment of Toxicity Reduction. *C* **2024**, *10* (2), 56. https://doi.org/10.3390/c10020056.

(116) Ishimaru, K.; Hata, T.; Bronsveld, P.; Nishizawa, T.; Imamura, Y. Characterization of Sp^2- and Sp^3-Bonded Carbon in Wood Charcoal. *J Wood Sci* **2007**, *53* (5), 442–448. https://doi.org/10.1007/s10086-007-0879-7.

(117) Fujimoto, H. Theoretical X-Ray Scattering Intensity of Carbons with Turbostratic Stacking and AB Stacking Structures. *Carbon* **2003**, *41* (8), 1585–1592. https://doi.org/10.1016/S0008-6223(03)00116-7.

(118) Li, Z. Q.; Lu, C. J.; Xia, Z. P.; Zhou, Y.; Luo, Z. X-Ray Diffraction Patterns of Graphite and Turbostratic Carbon. *Carbon* **2007**, *45* (8), 1686–1695. https://doi.org/10.1016/j.carbon.2007.03.038.

(119) Hassanzadeh-Tabrizi, S. A. Precise Calculation of Crystallite Size of Nanomaterials: A Review. *Journal of Alloys and Compounds* **2023**, *968*, 171914. https://doi.org/10.1016/j.jallcom.2023.171914.

(120) Yang, M.; Shu, X.; Zhang, J. A Defect-Rich N, P Co-Doped Carbon Foam as Efficient Electrocatalyst toward Oxygen Reduction Reaction. *ChemCatChem* **2020**, *12* (16), 4105–4111. https://doi.org/10.1002/cctc.202000363.

(121) Srinu, A.; Peera, S. G.; Parthiban, V.; Bhuvaneshwari, B.; Sahu, A. K. Heteroatom Engineering and Co–Doping of N and P to Porous Carbon Derived from Spent Coffee Grounds as an Efficient Electrocatalyst for Oxygen Reduction Reactions in Alkaline Medium. *ChemistrySelect* **2018**, *3* (2), 690–702. https://doi.org/10.1002/slct.201702042.

(122) Li, O. L.; Wada, Y.; Kaneko, A.; Lee, H.; Ishizaki, T. Oxygen Reduction Reaction Activity of Thermally Tailored Nitrogen-Doped Carbon Electrocatalysts Prepared through Plasma Synthesis. *ChemElectroChem* **2018**, *5* (14), 1995–2001. https://doi.org/10.1002/celc.201800063.

(123) Wang, N.; Lu, B.; Li, L.; Niu, W.; Tang, Z.; Kang, X.; Chen, S. Graphitic Nitrogen Is Responsible for Oxygen Electroreduction on Nitrogen-Doped Carbons in Alkaline Electrolytes: Insights from Activity Attenuation Studies and Theoretical Calculations. *ACS Catal.* **2018**, *8* (8), 6827–6836. https://doi.org/10.1021/acscatal.8b00338.

(124) Wu, B.; Meng, H.; Morales, D. M.; Zeng, F.; Zhu, J.; Wang, B.; Risch, M.; Xu, Z. J.; Petit, T. Nitrogen-Rich Carbonaceous Materials for Advanced Oxygen Electrocatalysis: Synthesis, Characterization, and Activity of Nitrogen Sites. *Advanced Functional Materials* **2022**, *32* (31), 2204137. https://doi.org/10.1002/adfm.202204137.

(125) Meng, Z.; Mo, R.; Wang, Q.; Zheng, K.; Li, W.; Qin, C. Nitrogen-Doped Porous Carbon Derived from Graphite of Solid Waste for Activating Peroxymonosulfate to Degradation Tetracycline. *Colloids and Surfaces A: Physicochemical and Engineering Aspects* **2023**, *662*, 130984. https://doi.org/10.1016/j.colsurfa.2023.130984.

Table of Contents Graphic and Synopsis